MICROCOPY RESOLUTION TEST CHART
NATIONAL BUREAU OF STANDARDS-1963-A

FOREIGN TECHNOLOGY DIVISION

JOURNAL OF ENGINEERING THERMOPHYSICS

(Selected Articles)

DTIC
ELECTE
S D
JUN 17 1983
D

83 06 16 085

FTD -ID(RS)T-0416-83

EDITED TRANSLATION

FTD-ID(RS)T-0416-83   13 May 1983

MICROFICHE NR: FTD-83-C-000666

JOURNAL OF ENGINEERING THERMOPHYSICS (Selected Articles)

English pages: 66

Source: Gongcheng Rewuli Xuebao, Vol. 2, Nr. 3,
              1981, pp. 224-261

Country of origin: China
Translated by: LEO KANNER ASSOCIATES
                        F33657-81-D-0264
Requester: FTD/TQTA
Approved for public release; distribution unlimited.

FTD -ID(RS)T-0416-83   Date 13 May 19 83

TABLE OF CONTENTS   Pages

i

GRAPHICS DISCLAIMER

All figures, graphics, tables, equations, etc. merged into this
translation were extracted from the best quality copy available.

AN INVESTIGATION* OF THE CHARACTERISTIC AND INSTABILITY BEHAVIOR OF AN AXIAL
COMPRESSOR IN A TURBOJET ENGINE

Inlet Distortion Research Group, Northwest Polytechnical University

In this paper, experimental results and analysis about the effect of the inlet pressure distortion, decrease in the first stage turbine nozzle area and engine test run program on the characteristic and instability behavior of an axial compressor in a turbojet engine are presented. The experiments have been conducted on the test bed on a turbojet engine with a 9-stage compressor, whose first stage is transonic.

The results show that: (1) inlet distortion and decrease in turbine nozzle area may shift considerably the speed lines of compressor leftward and cause it to become more flat in shape; (2) the different run program for engine test may produce different speed line of compressor both in position and shape; (3) at low and medium speed, the instability of compressor exhibits itself as a rotating stall, and at high speed, a surge, whose mode depends on the degree of inlet distortion and decrease in turbine nozzle area.

I. FOREWORD

The characteristic and instability behavior of a multistage axial
compressor is a problem of concern to design personnel, who not only have
to understand the characteristics of the axial compressor components during
the tests, but more important is to understand the characteristics of the
propulsion installation of the axial compressor or characteristics of the gas

---

*This paper was read at the Third All China Engineering Thermophysics Conference
at Guilin in April 1980.　　1

turbine installation in order to predict and analyze the matching among
components and characteristics of the entire machine. Besides, the design
personnel require to understand the instability behavior of a compressor
at the stall line in order to extensively study the cause of instability
of an axial compressor at the stall line in order to extensively study
the cause of instability of an axial compressor, prediction of unsteady
vibration, and prevention of unsteady vibration. This test was undergone
on a turbojet engine. The paper stresses the introduction of influence
of various factors on characteristics of an engine compressor and on
instability behavior. The testing revolution speed was run between 87 and
100 percent of the rated revolution speed. There are two types (of anomaly
meshes): one layer of 36 eyes, and three layers of 36 eyes. There are two
types of first stage nozzle area: one is the normal area at the design
stage, and the other is reduced by 12 percent. In addition, according to
different starting sequences, curves of equal revolution speed of 88.4 percent
of the designed revolution speed, and the operating points at 87, 90 and
93.3 percent of the designed speed were measured.

II. EXPERIMENTAL INSTALLATION AND EXPERIMENTAL METHOD

Figure 1 shows the test installation and schematic diagram for measure-
ment points. In front of the engine inlet at a distance of about 0.5 of the
diameter length, a rotatable metal mesh is installed to produce the required
square wave anomaly spectrum. A movable tail cone was installed behind
the nozzles of the engine in order to induce unsteady engine vibration.

While studying the effect of inlet anomaly and variation of the first
stage nozzle area of the turbine, the engine revolution speed was maintained
constant. The nozzle openings were changed and the tail cone moved to let
the operating points of the engine move at a constant revolution speed curve
until unsteady vibration or stall appeared.

In studying the influence of the starting sequence, starting was
conducted according to the following two sequences: one is accelerating from
idling revolution speed to testing revolution speed before throttling along
the equal revolution speed curve. Another is decelerating from the designed

2

revolution speed (the nozzle opening is in the accelerating state) to the testing revolution speed before throttling along the equal revolution speed curve.

III. RESULTS AND ANALYSIS

(A) Influence due to anomaly of inlet gas pressure
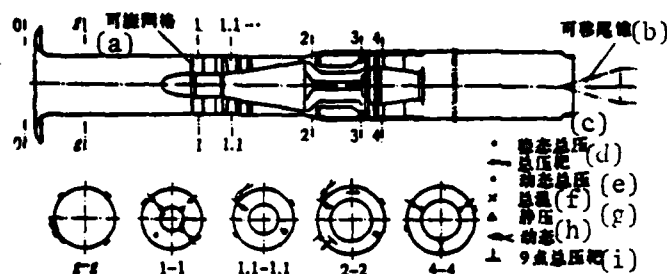
Fig. 1.   Schematic diagram of testing installation and testing point arrangement.
Key: (a) Rotatable mesh; (b) Movable tail cone;
(c) Total pressure in steady state; (d) Target of total pressure; (e) Total pressure in dynamic state;
(f) Overall temperature; (g) Static pressure; (h) Dynamic state; (i) Nine point target of total pressure.

While Figs. 2, 3 and 4 are, respectively, $\bar{n}=0.9$ and one layer with 36 eye mesh (covering circumferential angle at 180°), the pressure spectrum, total pressure circumferential spectrum and wall surface static pressure spectrum at the inlet cross section of the engine, the damping function of the mesh creates the circumferential anomaly spectrum of total pressure nearing a square wave; however, the suction function on a high and low pressure region gas stream by the compressor causes the static pressure anomaly as shown in Fig. 4.

Figure 5 shows the influence of engine compressor characteristics on the inlet gas anomaly while $\bar{n}=0.9$.   In the diagram, three equal revolution curves are shown for cases without mesh, one layer with 36 eye mesh (180° covering), and three layer mesh with 36 eyes (180° covering).   The dot and

3

dash curve shows the results of the compressor component test on a platform. In the diagram, three curves of equal nozzle area show, respectively, nozzle opening positions at acceleration (ϕ), rated power (H), and the maximum overload (M) condition.
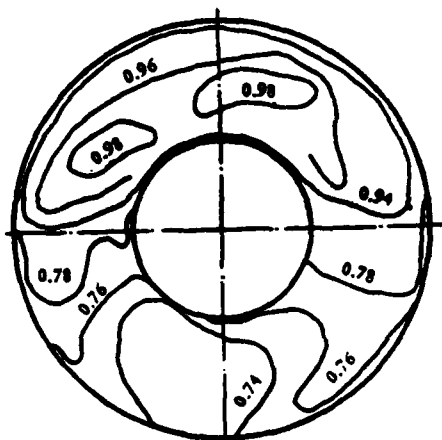
Fig. 2. Pressure spectrum at engine inlet.

Fig. 3. Total pressure circumferential spectrum at engine inlet.
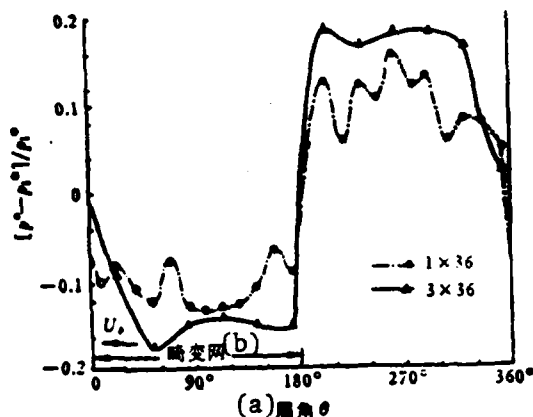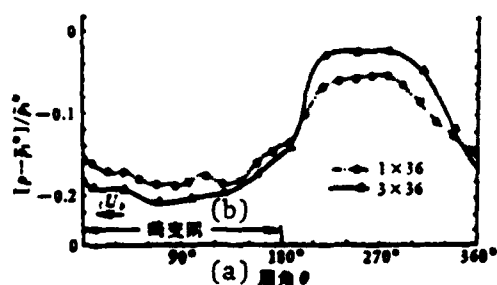Key: (a) Circumferential angle; (b) Anomaly mesh.

Fig. 4. Static pressure circumferential spectrum at engine inlet.
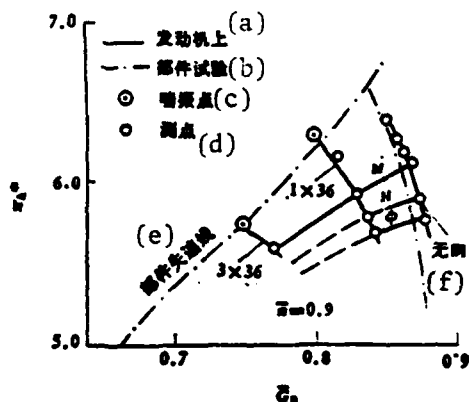Key: (a) Circumferential angle; (b) Anomaly mesh.

Fig. 5. Influence on engine compressor characteristics of inlet gas anomaly.
Key: (a) On engine; (b) Component test; (c) Point of unsteady vibration; (d) Measurement point; (e) Stall line of component; (f) Without mesh.

4

As revealed by the test results, the inlet gas anomaly moves leftward and levels the equal revolution speed curve; the greater the anomaly, the more pronounced is the variation. The main cause of "leftward motion" and "leveling" is possibly weakening of the toal circulating capacity of the compressor with reduction in total flow and intensifying of perturbation between stages (lowering of efficiency and reduction of pressure ratio). The experimental results also reveal that the inlet gas anomaly reduces the allowance of unsteady vibration as shown in Fig. 5. Owing to leftward motion and leveling of the equal revolution speed curve, the lowering allowance of unsteady vibration is the overall result of simultaneous lowering of pressure ratio and flow.

Figure 6 gives the characteristics of two (anomaly and "net") sub-compressors and the average characteristics of the whole compressor set. It is apparent from the figure that before unsteady vibration of the compressor, the pressure ratio of the anomaly subcompressor exceeds the pressure ratio of stability state unsteady vibration. This is because in an anomaly flow field, the rotor blades are undergoing periodic variation of the gas stream attack angle. Under this instability state, the proved phenomenon of lagging dynamic stall (larger attack angle can be borne by the blades than in the stability state without stall) to let the operating pressure ratio of the anomaly subcompressor exceed the stability state pressure ratio (of unsteady vibration) while the compressor still maintains a steady operation.

Figures 7 and 8 show, respectively, the situation of engine unsteady vibration at two different anomalies for the time duration of compressor exit total pressure p_2^* and the static pressure p_s of the flow measurement sector. It is apparent by comparing two diagrams that the anomaly degree has an effect on the unsteady state of the gas stream. It can be considered that the "classical unsteady vibration" appears for three layer 36 eye mesh, and "deep unsteady vibration" appears for one layer 36 eye mesh. Figure 9 (with operating condition the same as that of Fig. 7) shows the photograph of a mesh having fallen down by reverse shock of the shock wave during unsteady vibration of the engine.

5
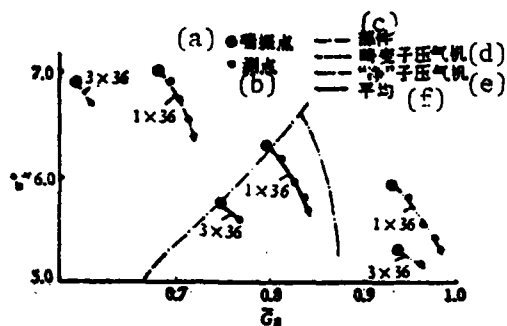
Fig. 6. Compressor characteristics of anomaly engine
Key: (a) Point of unsteady vibration; (b) Measurement point; (c) Component; (d) Anomaly subcompressor; (e) "Net" subcompressor; (f) Average.
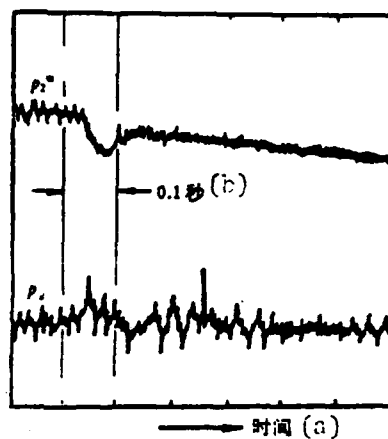
Fig. 7. Time duration of p_2^* and p_g with unsteady vibration of the engine at 1x36 eye mesh.
Key: (a) Second; (b) Time.
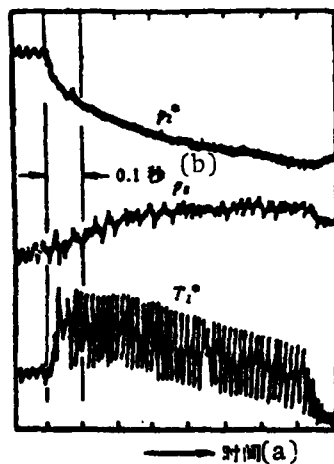
Fig. 8. Time durations of p_2^*, p_g and T_2^* for unsteady vibration of the engine with a 3x36 eye mesh.
Key: (a) Time; (b) Second.
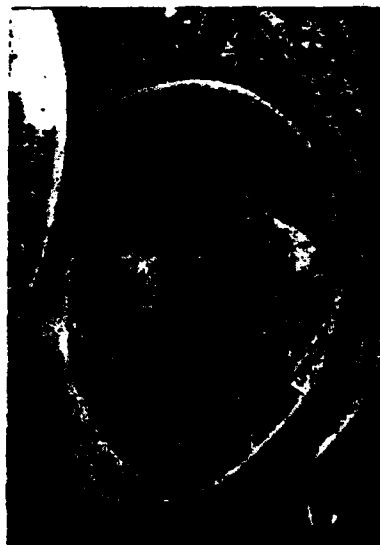
Fig. 9. Photograph of a mesh falling down, by a shock wave during unsteady vibration.

6

(B) Influence of first stage nozzle area of the turbine.

Figure 10 shows the variation of engine compressor characteristics when the first stage nozzle area of a turbine is reduced by 12 percent. Reduction of first stage nozzle area moves the operating points of the engine upward; the compressor equal revolution speed lines move leftward and become level; the lower the revolution speed, the more level are the equal revolution speed curves, even appearing with the left branch of the revolution speed curves at slightly positive values of the inclination. Figure 11 shows the time durations of p_2^*, p_g and T_2^* (with $\bar{n}=0.87$) undergoing unsteady vibration when the first stage nozzle area is reduced by 12 percent. It is apparent from the diagram that the shock wave produced during unsteady vibration arrives at the flow measurement sector within approximately 6 to 8 milliseconds. At that time, a peak value of p_g appears. According to analysis, the unsteady state is the "deep unsteady vibration".

(C) Influence of starting sequence

Figure 12 shows the equal revolution speed curves of $\bar{n}=0.884$ measured at different starting sequence and the operating points of $\bar{n}=0.933$, 0.9 and 0.87. The small black circles in the diagram show the measurement values from idling revolution speed accelerating to the testing revolution speed; the small white circles represent the measurement values from design of revolution speed expanding nozzle area decelerating to the testing revolution speed. From the limited data shown in the diagram, it is apparent that we can see the "multiple" characteristics of the equal revolution speed curves of the axial compressor; i.e., different equal revolution speed curves can be obtained with different manners of starting. The appearance of "multiple" characteristics may possibly be related to the "lagging phenomenon" of rotational stall and interstage perturbation of the axial compressor.

(D) Influence of engine revolution speed

The engine revolution speed is one of the major factors affecting the unsteady state of a compressor. As revealed by considerable analyses and experimental studies, during low speed generally rotational stall appears on

the engine at the stabilized boundary. However, during high revolution speed, unsteady vibration frequently occurs. This study also proves this point.
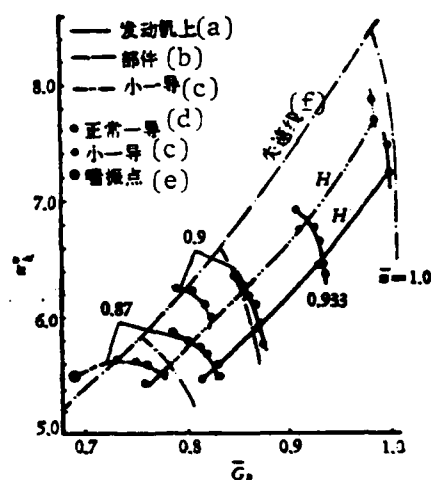
Fig. 10. Influence of compressor characteristics by reducing 12 percent of the first stage nozzle area while $\bar{n}=0.87$.
Key: (a) On engine; (b) Component; (c) Small nozzles for the first stage; (d) Normal nozzles for the first stage; (e) Point of unsteady vibration; (f) Stall curve.
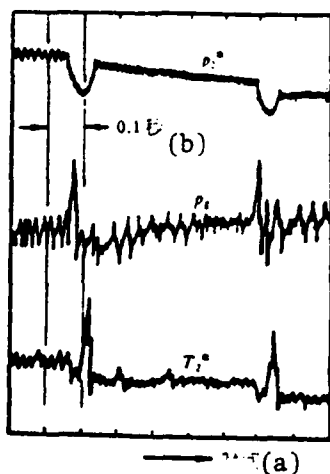
Fig. 11. Time durations of p_2^*, p_g and T_2^* during unsteady vibration while the first stage nozzle area is reduced by 12 percent.
Key: (a) Time; (b) Second.
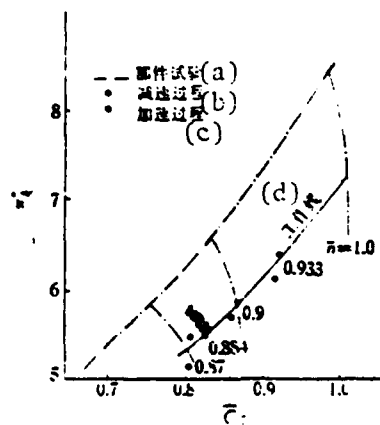
Fig. 12. Influence on engine compressor characteristics of starting sequence.
Key: (a) Component test; (b) Decelerating process; (c) Accelerating process; (d) Operating curve.

8

Figure 13 shows the behavior overtime of p_2^*, T_2^* and pg and interstage $p_{1.1}^*$ and $p_{1.3}^*$ when n = 0.69 (called "upper breathing point) at stall; the frequency is 46 percent of the rotational speed. It is so-called "lower point of un-steady vibration")`. However, when $\bar{n}$=0.87, the unsteady state appeared as "deep unsteady vibration"shown in Fig. 11.

——➤ 时间 *
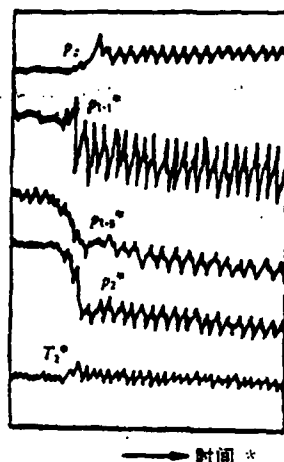
Figure 13. The behavior overtime of pg, $P_{1.1}$, $P_{1.3}$, P_2^*, and T_2^* when $\bar{n}$=0.69 and at stall.
Key: (*) Time.

The problem of unsteady vibration of a compressor can be analyzed by using the Helmholtz acoustical resonator model. During unsteady vibration of the compressor, the gas stream vibrates at the front and rear; while using a resonator, the gas column vibration at the neck portion becomes a model. The motion equation of the gas column at the neck portion of the resonator can be written as [3]:

$$\frac{d^2x}{dt^2} + a^2\left(\frac{A_c}{V_pL_c}\right)x = 0$$

Obviously, the vibration frequency (of the gas column)

$$\omega = a\sqrt{A_c/V_pL_c}.$$

In the equation, a is the sound speed; A_c is the equivalent area of the compressor ring surface; V_p is the volume behind the compressor; and L_c is the equivalent length of the compressor.

9

$$B = U/2\omega L_c = (U/2a)[\sqrt{V_p/A_c L_c}]$$

Through experiments and analyses, Greitzer [4, 5] proved the existence of a critical value $B_{critical}$. When $B < B_{critical}$, rotational stall appears at the steady boundary; unsteady vibration appears when $B \geqslant B_{critical}$. It is apparent from the above equation that the value of B is determined by the rotational speed for a machine of a definite structure. Therefore, unsteady vibration easily occurs at high revolution speed. Rotational stall often appears during low rotational speed. In the result of this experiment, it is the abrupt type stall while $\bar{n} \leqslant 0.69$ ($B \leqslant 0.79$); it is the unsteady vibration when $\bar{n} \geqslant 0.87$ ($B \geqslant 0.98$).

It should be pointed out that by using the Helmholtz resonator model, the actual system of the influences on the unsteady state by the following factors is not considered: position of throttling valve, inlet gas anomaly, and operating point positions of compressor. However, for rotational speed, the revelation trend of the above mentioned expression equations is consistent with the experimental results.

IV. CONCLUSIONS

(1) For an axial compressor inside a turbojet engine, the characteristics are not only determined by the characteristics of the compressor components, but are also related to the structure layout and operating conditions of other components in the compressor system. The inlet gas anomaly and reduction of the first stage nozzle area of the turbojet engine can move leftward and become more level for the equal revolution speed curves; the lower the revolution speed, the more pronounced is the leftward motion and leveling. A different starting sequence also will cause variation to the shape and position of the equal revolution speed curves.

(2) The unsteady state appearing at the steady boundary of the turbojet engine compressor is mainly determined by volume and revolution speed of the combustion chamber. At the same time, the unsteady state is related to operating conditions and the system of the compressor. At $\bar{n} \leqslant 0.69$ for the

10

turbojet engine in the experiment, the appearing unsteady state is the abrupt type stall; during $\bar{n} \geqslant 0.87$, it is the unsteady vibration. In these situations, "classical unsteady vibration" appears when three layers of 36 eye mesh appear. While the first stage nozzle area of the turbojet engine is reduced by 12 percent, the "deep unsteady vibration" appears.

(3) Due to lagging of the dynamic stall, the operating pressure ratio of the subcompressor during low inlet gas pressure may exceed the pressure ratio of stability state unsteady vibration of a homogeneous inlet gas.

The experiment of this paper was collectively completed by the Inlet Distortion Research Group.

LITERATURE

[1] Demetrius Zonars: Dynamic Characteristic of Engines Inlets, AD-744595, (1974).
[2] Susumu Nagano: Rotating Stall in a 5-Stage Transonic Compressor, AD/A 003853, (1974).

3. Aleksandrovitch, A. D., Matematika eye soderzhaniye, Metody i enacheniye [Mathematics, its Contents and Significance], Vol. 2, USSR Academy of Science Publishing House, 1956.

[4] Greitzer, E.: Surge & Rotating Stall in Axial Flow Compressor. Pt I. Theoretical Compression System Model. Trans. of ASME. (April, 1976).
[5] Greitzer, E.: Surge & Rotating Stall in Axial Flow Compressor. Pt II. Experimental Results & Comparision With Theory, Trans. of ASME, (April 1976).

PREDICTION* OF ONSET OF ROTATING STALL USING SMALL PERTURBATION THEORY FOR AXIAL FLOW COMPRESSORS

Liu Zhiwei**

Northwest Polytechnical University

This paper analyses, generalizes and compares different onset conditions of the predicting rotating stall, which are based on small perturbation theory. They are correlated to experimental data of rotors for single stage axial flow compressors. Good agreement between theoretical values and experimental values is found. Mechanism for the onset condition of rotating stall is analysed. Effectiveness of methods of prediction is proved. The extent of application of methods is extended.

I. FOREWORD

The prediction of onset of rotating stall is related to the determination of the allowance index and compressor stall boundary. Up to now, there is still no method to be followed. Starting from different viewpoints, quite a few sources of information proposed the basis of evaluating the methods. It seems that those conclusions do not have generalized significance owing to lacking of more experimental data. Or, it is difficult to more accurately

---

determine the empirical formula because of too great a range of the empirical data. It seems that the criterion established by analyzing the stability of fluid passing through the blade array on the basis of small perturbation theory can basically get to the nature of the problem. In addition, good agreement between the theoretical and experimental values can be obtained. The work of this aspect has been proven by G. R. Ludwig et al [1].

Noticing different premises and treatment methods of several small perturbation theories in analyzing the fluid stability, there are different criteria in predicting stall onset conditions. In addition, on viewing the data in [1] correlating only at a low M number (smaller than 0.2) and large hub ratios, the influences of fluid compressibility and three-dimensional effects are considerably different than for rotors used in practice. In order to discuss the effectiveness in practical applications of the above-mentioned theoretically obtained criteria, in this paper correlation is made between rotor data and theory for comparing various types of small perturbation theories in analyzing the stall onset points. This goes a further step in proving the effectiveness of predicting the onset of a rotating stall of a single blade array; the range of application is extended.

II. ANALYSIS OF SMALL PERTURBATION THEORY

It is assumed that the passing through the blade array by the gas stream is two-dimensional, incompressible and unsteady, and the blade array is substituted by a model of an excitation disc as shown in Fig. 1. At the same time, it is assumed that the perturbation amount of the gas stream can be neglected compared to the corresponding average gas flow. This is the assumption of small perturbation.

From the method of solving for the perturbation amount of upper and lower streams of a flow field of the blade array, the small perturbation theory can be divided into two categories: one is the series form solution in perturbation speed potential function at the upper stream of the blade array in order to obtain the onset conditions of evaluating the rotating stall [2]. Another category is the multiple index form flow function at the upper and lower

13

stream blade array to obtain the onset conditions of evaluating the rotating stall [1, 3, 4].

In order to obtain the solution of the second category flow function, in this paper a motion equation of perturbation vorticity describes the flow fields at the upper and lower streams of the blade array.

$$\frac{\partial \zeta}{\partial t} + (U + u)\frac{\partial \zeta}{\partial x} + (V + v)\frac{\partial \zeta}{\partial y} = 0 \quad (1)$$

Under the given onset conditions and boundary conditions, the perturbation vorticity expressed in the form of a multiple index can be obtained:

$$\zeta = \zeta_0 e^{[i\zeta_t + i\frac{s}{r}\,y - i\frac{s}{r}\,x(\frac{C_r}{s_0} + \mathfrak{z}_i)]} \quad (2)$$

By relating the perturbation flow function and perturbation vorticity satisfying the continuity equation, we get:

$$\nabla^2 \Psi = -\zeta \quad (3)$$

Substitute eq. (2) into eq. (3) and after variable replacement, the solution in the form of Poisson's equation can be derived, in obtaining the expression equation with the same form as the perturbation flow function in [3]:

$$\Psi_i = A_i e^{[i\zeta_t - \frac{s}{r}(x - h)]} + B_i e^{[i\zeta_t + \frac{s}{r}(x + h)]} + D_i e^{[i\zeta_t + i\frac{s}{r}\,y - i\frac{s s}{r}\,(\frac{C_r}{s_0} + \mathfrak{z}_i)]} \quad (4)$$

If the same coordinating and boundary conditions are used as in [1], the homogeneous equation set of the unknown constants A_i, B_i and D_i can be obtained. According to conditions of non-singular solution of this equation set, one root of the physical significance of the characteristic equation can be determined, thus obtaining the onset conditions of a rotating stall as pointed out in [1]:

When $p_2(\infty, y)$=constant, the damped factor is:

14

$$\frac{rC_1}{nU} = \frac{1}{2+g}\left\{1 + X + S_1^2 + S_1^2(1 - S_1S_2) - \frac{S_1}{2}(1 + S_1^2)X'\right\} \qquad (5)$$

And when $p_2(0^+, y)$=constant, the damped factor is:

$$\frac{rC_1}{nU} = \frac{1}{2+g}\left\{1 + X + S_1^2 - S_2'S_1S_2 - \frac{S_1}{2}(1 + S_1^2)X'\right\} \qquad (6)$$

If $C_1 > 0$, the gas stream is stabilized; if $C_1 < 0$, the gas stream is not stabilized; if $C_1=0$, this is the neutral stabilization condition. From eq. (5) or eq. (6), the onset point of a rotating stall can be determined.

For comparison, conclusions of various methods should be homogeneous. This paper conducts further analysis of the onset conditions in [3] and [4].

From [3], the onset condition is:
$$\xi' = 2(\xi + \cos^2\beta_2)/ctg\,\beta_1 \qquad (7)$$

In addition, it is noted that $\xi = X(1 + ctg^2\beta_1)$ and $\xi' = \partial\xi/\partial ctg\,\beta_1$, then

$$1 + X + S_1^2 - [S_1(1 + S_1^2)X'/2] = 0 \qquad (8)$$

If the influence of time lag of the adhering layer is neglected, and from [4] it is determined that the increment rate is equal to zero to determine the stall onset point, similarly, the same expression equation as eq. (8) can be obtained, thus determining that there is no inherent difference in the linear theoretical part.

Comparing eq. (5) or eq. (6) with eq. (8), it is apparent that eq. (8) is the special case of the two other equations. If the variation of exhaust angle with gas inlet angle is not considered, these equations have the same form. The basic cause of their differences is the diversion characteristics of the blade array.

III. SOLVING EXPERIMENTAL PROBLEMS

15

Using correlated comparison between the analysis results and four rotor
data, there are the isolated rotor data (variable energy design of the
rotor along the blade height) and the rotor data provided in [5-7] of a medium
hub ratio of the simultaneous experiment.   In correlation, influence on the
rotor is not considered.   The related parameters of these test pieces are
compiled in Table 1.

Table 1.   Rotor parameters

参 数 (a) \ No.	(b) 自 行 试 验	[5]	[6]	[7]
(c 压 比	1.25	1.20	1.20	1.53
叶尖来流相对 M 数 (d)	0.78	0.87	0.88	1.2
(e 轮 毂 比	0.61	0.46	0.42	0.40
展 弦 比 (f)	1.94	1.78	3.28	6.28
(g 安 装 角°	48.2°	72.8°	62.3°	53.6°
弯 角 (h)	42.6°	39.5°	22.3°	21.6°
(i 稠 度	1.17	0.998	1.623	1.881

* All parameters related with the cross section mean the arithmetic
mean parameters for an average radius.
Key: (a) Parameters; (b) Author's experiments; (c) Pressure ratio;
(d) Relative M number of incoming flow at the blade tip; (e) Hub
ratio; (f) Aspect ratio; (g) Installation angle*; (h) Bending angle;
(i) Viscosity.

Data compilation method: The average parameters of a gas stream passing
through the rotors are substituted by mass average parameters.   The geometrical
characteristics cross section of rotors is selected for the average radius of
the area.   The data compilation progresses on the assumption of cylinder flow.
The loss characteristic of the rotor blade array is calculated according to
the following equation.

$$X = (p_{2\infty}^* - p_2^*)/(p_{2\infty}^* - p_1) \qquad (9)$$

The diversion characteristic is obtained by averaging the measured distribution
parameters along the blade height.   Figure 2 lists the average characteristics
of subsonic rotors in the author's experiments and the transonic rotor provided
by [7].   There is no repetition for characteristics of other rotors because
of similarity.

16

Processing of experimental data: In Fig. 2, the inlet gas angle
is reduced to the flow pattern that the rotating stall will immediately
appear; however, flow is still maintained at the corresponding point of
normal stabilized flow, i.e., the so-called neutral stabilized boundary
point. This is the stall boundary point as it is usually meant. The inlet
gas angle corresponding to this point is the inlet gas angle of the onset
point of a rotating stall determined by the experiment. For an abrupt type
rotating stall, the blade array characteristic curve after the neutral
stabilized boundary point will have interruption point. After the curve
passes through the interruption point, the natural extension is the approximate
processing method in data correlation. Data processing is done according
to the method of least squares for the characteristics of various rotors. In
addition, the following polynomial is taken for curve simulation.

$$\begin{cases} \ddot{x} = a_0 + a_1 S_1 + a_2 S_1^2 \\ S_2 = a_3 + a_4 S_1 + a_5 S_1^2. \end{cases} \tag{10}$$
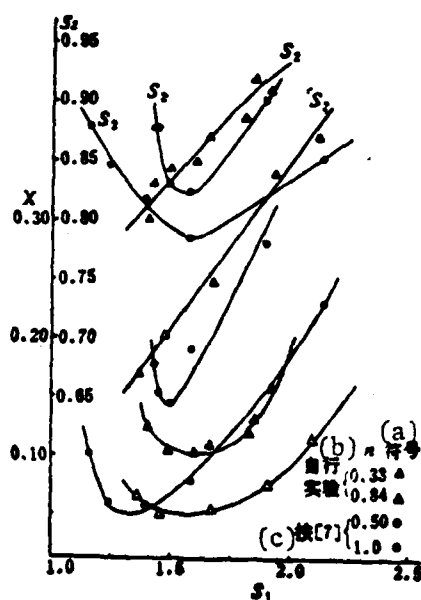
Fig. 2. Average characteristics of subsonic
and transonic rotors.
Key: (a) Symbol; (b) Author's experiments;
(c) According to [7].

17

IV. RESULTS OF CORRELATION BETWEEN EXPERIMENTS AND THEORY

The rotor characteristics after processing are substituted into eq. (5) or (6), and eq. (8). The corresponding inlet gas angle at onset of the theoretical rotating stall is obtained; comparison is made between the theoretical and experimental values. Figure 3 lists curves of the damped factors rC_1/nU (varying with S_1) calculated with correlation using the author's experiment data and eq. (5). It is apparent from Fig. 3 that good agreement exists between the theoretical and experimental values.
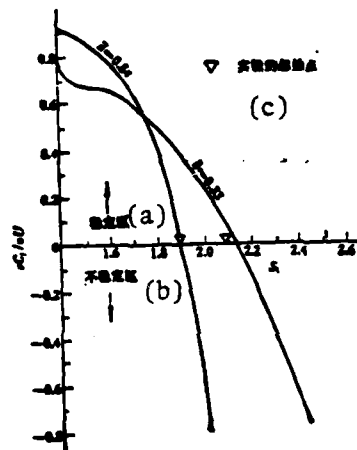
Fig. 3. Theoretical stability characteristic [using eq. (5)] of rotors.
Key: (a) Steady region; (b) Unsteady region; (c) Onset point of experiment.

Tables 2 and 3 list, respectively, the rotor data according to the author's experiment and using [5-7] and adopting eq. (5) or eq. (6) for the correlation calculation in obtaining the onset inlet gas angle and the corresponding experimental value. Table 4 lists the compared results of two rotors with the above-mentioned (similar) calculation using eq. (8).

From comparison of four rotors listed in the tables mentioned above, it is apparent that: Notwithstanding the considerable difference in geometrical parameters and performance characteristics of the rotor, there is good

18

Table 2. Comparison of theoretical value [according to eq. (5) and eq. (6)] of the onset point inlet gas angle.

$\bar{z}$	(a) 实验值 β_{1s} (度) (c)	(b) 理论值 β_{1s} (度)(c)		(d) 相对误差百分数 $\triangle\%$		失速团数 (e) n (实验和理论) (g)
		$p_2(\infty, y) = $ 常数 (f)	$p_2(0^+, y) = $ 常数 (f)	$p_2(\infty, y) = $ 常数 (f)	$p_2(0^+, y) = $ 常数 (f)	
0.33	25.5	25.0	25.5	1.9	0	1
0.54	25.9	25.7	26.1	0.75	0.60	1
0.71	27.3	27.0	27.2	0.96	0.35	1
0.84	27.7	26.9	27.1	2.9	2.4	1

Key: (a) Experimental value; (b) Theoretical value; (c) Degree; (d) Relative error percentage; (e) Number of stall groups; (f) Constant; (g) Experiment and theory.

Table 3. Comparison of theoretical value [according to eq. (5)] and experimental value of the onset point inlet gas angle.

(c) 按 [5] $\bar{z}$ \ β_{1s} (度) (a)	理论值 (b)	实验值 (c)	(d) 按 [6] $\bar{z}$ \ β_{1s} (度) (a)	理论值 (b)	实验值 (c)	(d) 按 [7] $\bar{z}$ \ β_{1s} (度) (a)	理论值 (b)	实验值 (c)
0.8	37.9	40.9	0.8	33.2	32.7	0.5	27.5	25.1
0.9	41.8	42.6	0.9	37.8	37.6	0.7	27.5	25.9
1.0	43.7	43.2	1.0	34.6	32.9	0.8	27.4	27.4
			1.1	34.8	34.6	1.0	29.0	27.9

Key: (a) Degree; (b) Theoretical value; (c) Experimental value; (d) According to.

Table 4. Comparison of theoretical value [according to eq. (8)] of the onset point inlet gas angle.

(a) 按自行实验数据 $\bar{z}$ \ β_{1s} (度) (b)	(c) 理论值	(d) 实验值	(e) 按 [7] $\bar{z}$ \ β_{1s} (度) (b)	(c) 理论值	(d) 实验值
0.33	24.5	25.5	0.5	26.8	25.1
0.54	25.1	25.9	0.7	27.2	25.9
0.71	26.9	27.3	0.8	26.8	27.4
0.84	26.8	27.7	1.0	28.3	27.9

Key: (a) According to data in author's experiments; (b) Degree; (c) Theoretical value; (d) Experimental value; (e) According to.

agreement between the inlet gas angle at stall onset; their relative error is within 5 percent except in individual points as high as 10 percent. Secondly, differences are brought about by the onset criterion of the boundary condition at the lower stream of different blade array outlets; there is no major influence in estimating the theoretical values. Thirdly, as revealed in the correlation comparison of eq. (5) and eq. (8), results of the two are satisfactory. This explains that the diversion characteristic of the blade array is secondary in evaluation of the onset point; however, the loss characteristics have a determined function; this has a restraining effect on the diversion characteristics. In other words, the instability factor of the blade array is mainly determined by the related term of the loss variation rate X'. The term related to the exhaust gas angle variation rate S_2' may be a steady factor, and may be an unsteady factor. However, the influence on stall onset point is very slight, even to a negligible degree. Attention is necessary that the diversion capability of the blade array and the loss itself created are the factors maintaining the stability.

As revealed by the data correlation described above, although there are unavoidable three-dimensional influences existing among various rotor blade arrays, however, this three-dimensional characteristic does not play an important role in the prediction of a rotating stall. In addition, an average blade array characteristic can be found as representation to predict the stall onset point. It is also indicated that the fluid compressibility has a secondary position in the influence of stall onset conditions. This can be determined by going a further step, by taking into account the reliability degree and adaptation range of the prediction theory of two-dimensional incompressible unsteady small perturbation of fluid inertia in the blade grid passage but neglecting the lagging of the adhering layer.

It should be point out that the theory of predicting the stall onset mentioned above is derived from the appearance of a rotating stall flow pattern. However, in practice often not a single unsteady flow pattern appears along the blade height to a rotor blade array; this is a blended unsteady flow pattern of a rotating stall and unsteady vibration. In this situation, this is a problem worth discussing in theoretically predicting

20

how effective it is. On this point, detailed measurements were made on dynamic characteristics of unsteady state points of rotors of the author's experiments. The results are shown in Figs. 4 and 5.
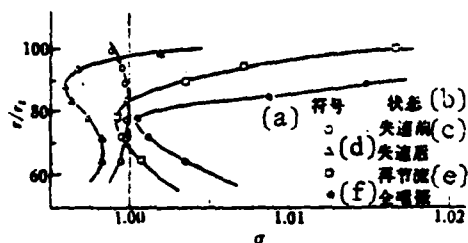

Fig. 4. Variation of circumferential time averaged total pressure restoration coefficient along the blade height at the rotor inlet when $\bar{n}=0.33$.
Key: (a) Symbol; (b) State; (c) Before stall; (d) After stall; (e) Throttling again; (f) Complete unsteady vibration.
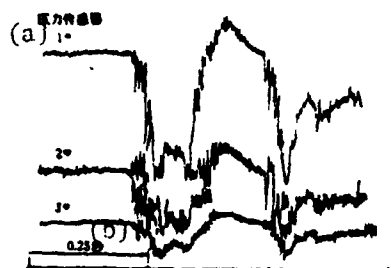
Fig. 5. Dynamic waveform of rotor with appearance of unsteady flow pattern when $\bar{n}=0.84$.
Key: (a) Pressure transmitter; (b) Second.

Figure 4 qualitatively explains the distribution of loss of inlet energy along the blade height before and after stall. In the rotating stall region of the blade height, all the restoration coefficients of the total pressure are smaller than the restoration coefficients of total pressure during normal flow. However, the closer to the portion of the blade tip $(r/r_x \geq 0.97)$, the greater the restoration coefficients. This explains that there is energy input into the sector. The energy comes from the reverse direction flow of the outlet. This indicates that after a stall there exists the blending of two flow patterns (rotating stall and unsteady vibration) along the entire blade height. At the same time, it is apparent from the diagram that with increasing throttling, the proportion occupied by the reverse direction flow region along the blade height is increased until the complete disappearance of the rotating stall and the flow pattern (of unsteady vibration) occupies all the blade height region. This can explain (by going a further step) the interrelated situation and conversion feature of the unsteady flow pattern.   21

Figure 5 shows that the low frequency oscillation of approximately 4 to 5 hertz is that of an unsteady vibration wave, carrying the rotating stall wave with frequency approximately at 120 hertz. However, the first appearance of the rotating stall wave can still be seen. Approximately 0.4 second later, a low frequency unsteady vibration wave then appears. As revealed by results correlating with this blending unsteady flow pattern, there is a good agreement between the theoretical prediction and experimental results. This seems to explain that the above mentioned linear prediction theory can be extended to the evaluation of an unsteady flow pattern.

V. CONCLUSIONS

By establishing the stability criterion of analyzing the fluid passing through the blade array on the basis of small perturbations, a generalized expression equation (5) or (6) can be derived. Criteria of other forms can be considered as special cases. By analyzing the stall onset point using the two dimensional, incompressible and unsteady flow model, it can be effectively applied to the correlation of actual compressor rotor data; the average performance can be used as the basis of correlation. The three-dimensional characteristic and compressibility have little influence on the stall onset conditions. In the regime of controlling the onset of a rotating stall, the average loss characteristic of the rotor similarly plays a dominant role. To the appearing situation of a blending unsteady flow pattern, the above mentioned criterion seems feasible to be applied. More experimental data are required for proof.

As revealed by the above mentioned results, it is possible in analysis of the criterion basis that the prediction skill of compressor unsteady boundary and stall allowance can be developed.

Symbols

a_i (a) 多项式系数 ($i = 0, 1\cdots5$)

A_i, B_i 和 D_i 流函数解中的常数 (c)

b (b) 叶片弦长 (d)

C 扰动涡度解中的复指数 (e)
$C = C_R + jC_I$

C_I, C_R 分别为 C 的虚部和实部 (f)

g (g) 组合参数, $g = b\pi\cos\gamma/r$

j (h) 虚数单位, $j = \sqrt{-1}$

m 失速团数目 (i)

$\bar{n}$ 设计转速的百分数 (j)

p_i i 区域中气流的静压 (k)

p_i^* (l) 区域中气流的总压

$p_{i\infty}^*$ (m) 区域中气流相对于动叶排的总压

r 叶排基元半径 (n)

s_i (o) i 区域中叶排的相对进气角的余切, $s_i = \text{ctg}\,\beta_i$

s_i' $s_i' = \partial s_i / \partial s_i$

$\bar{s}_i$ (p) i 区域中叶排的绝对进气角的余切 $\bar{s}_i = \text{ctg}\,\alpha_i$

t (q) 相对于叶片固定坐标的时间变量

u (r) 气流扰动速度的 x 向分量

U (s) 气流平均速度的 x 向分量

v 气流扰动速度的 y 向分量 (t)

V 气流平均速度的 y 向分量 (u)

X 总压损失系数 (v)

x, y (w) 固定于叶片上的坐标变量, x 沿轴向, y 沿切向

X' $X' = \partial X / \partial s_i$

β_i 相对气流角(与切向)(x)

γ 基元叶排叶片安装角(与切向)(y)

ζ 气流的扰动涡度 (z)

ξ (aa) 按进口动压头的轴向分量定义的总压损失系数

σ 进口总压恢复系数 (ab)

Ψ (ac) 气流的扰动流函数

下标: (ad)

i 气流区域 (ae)

s 旋转失速起始条件下的 (af)

t 叶尖的 (ag)

1 叶排进口区域的 (ah)

2 叶排出口区域的 (ai)

Key: (a) Polynomial coefficient; (b) And; (c) Constants in solution of flow function; (d) Length of blade chord; (e) Multiple index in solution of perturbation vorticity; (f) Respectively the virtual and real portions of C; (g) Combination parameter; (h) Unit of virtual number; (i) Number of stall groups; (j) Percentage of design revolution speed; (k) Static pressure of gas stream in region i; (l) Total pressure of gas stream in region i; (m) Total pressure of gas stream relative to the moving blade in region i; (n) Radius of an element in the blade array; (o) Cosecant of relative inlet gas angle of blade array in region i; (p) Cosecant of absolute inlet gas angle of blade array in region i; (q) Time variable relative to stationary coordinates of blades; (r) X direction component of perturbation speed of gas flow; (s) X direction component of average velocity of the gas stream; (t) Y direction component of perturbation speed of gas stream; (u) Y direction component of average speed of gas flow; (v) Loss coefficient of total pressure; (w) Coordinate variables fixing on blades: x along the axial direction and y along the tangent direction; (x) Relative gas flow angle (and tangent direction); (y) Blade installation angle (and tangent direction) of an element blade array; (z) Perturbation vorticity of gas stream; (aa) Loss coefficient of total pressure of axial component definition of dynamic pressure head at inlet;

23

[Continuation of Key of a table in the previous page]

(ab) Restoration coefficient of total pressure at inlet; (ac) Perturbation
flow coefficient of gas stream; (ad) Subscripts; (ae) Region of gas flow;
(af) Of rotating stall onset condition; (ag) Of blade tip; (ah) Inlet region
of blade array; (ai) Outlet region of blade array.

LITERATURE

[1] G. R. Ludwig, J. P. Nenni and R. H. Arendt: Investigation of Rotalling Stall in Axial Flow
Compressors and the Development of a Prototype Rotating Stall Contral System, AFAPL-TR-
73-45, (1973).

[2] H. W. Emmons, C. E. Pearson and H. P. Grant: Compressor Surge and Stall Propagation,
ASME Paper No. 53-A-65, (1954).

[3] Whitehead, D. S. Ph. D. Thesis: The Aerodynamics of Axial Compressor Blade Vibration. Cam-
bridge University, (1957).

[4] Saburo and H. Takata: Nonlinear Analysis of Rotating Stall. ISAS Report No. 449. 35, 7,
(1970).

[5] George W. Lewis and George Kovich: Overall and Blade Element Performance of a 1.20
Pressure Ratio Fan Stage with Rotor Blades Reset —7°, NASA TM X-3342, (1976).

[6] George W. Lewis, Jr. and Royce D. Moore: Aerodynamic Performance of a 1.20 Pressure Ratio
Fan Stage Designed for Low Noise, NASA TM X-3430, (1976).

[7] Lonnie Reid and Edward R. Tysl: Performance of a Transonic Compressor Rotor with an Aspect
Ratio of 6.5, NASA TN D-7662, (1974).

SOME CONSIDERATIONS CONCERNING THE PRINCIPAL EQUATION FOR THE AERODYNAMIC CALCULATION OF THE NON-RADIAL CALCULATION STATION ON S$_2$ STREAM-SURFACE FLOW IN TURBOMACHINES

Zhang Yujing

Harbin Marine Boiler and Turbine Research Institute

Received 10 October 1980

Based on Wu's equations expressed in terms of non-orthogonal curvilinear coordinates, this paper derives a y-direction equation of motion for the aerodynamic calculation of the non-radial calculation station on the S$_2$ stream-surface flow in a turbomachine blade passage. Thereby it is proved that the equation applied by Hetherington (1974) is correct. By means of transformation, it is pointed out that the principal equation (9) of this paper is in full agreement with the equation (11) of [2].

In aerodynamic calculation of the S$_2$ stream surface of turbomachines, while computation stations are non-radial direction computation stations within the gap of blade arrays, in 1974 Heterington used the following equation (see equation (30) in [1]):

$$\frac{1}{\rho}\frac{\partial p}{\partial y} = \frac{-W_y^2}{1-M_m^2}\left\{(1-M_y^2)\left(\frac{d^2y}{dz^2}\right)_+ - \frac{1}{2}\frac{\partial\tan^2\beta}{\partial y} - \frac{\tan\beta}{r}(\sin\varepsilon + \tan\beta\cos\varepsilon)\right\}$$
$$+ \frac{V_\theta^2}{r(1-M_m^2)}[(1-M_z^2)\cos\varepsilon + M_z^2\tan\beta\sin\varepsilon] \qquad (1)$$

The definition of the (y,z) coordinate system and angles ε and δ used are shown in Fig. 1*.

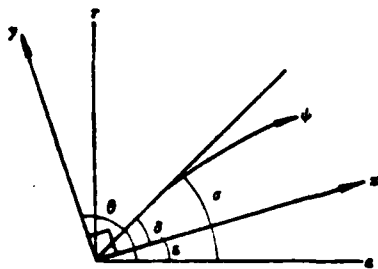Manuscript [2] expressed disagreement on the correctness of equation (1).

Fig. 1. (y,z) coordinate system used in equation (1).

Starting from the three-dimensional flow fundamental equation [3] of turbomachines with arbitrary curve coordinates, the paper derives the y direction motion equation for calculation of the S_2 flow surface of the (y, z, ϕ) coordinate system shown in Fig. 1; a proof was given that equation (1) is correct. By transformation, it is pointed out that the principal equation (9) derived is in agreement with equation (11) of manuscript [2].

DERIVATION OF Y DIRECTION MOTION EQUATION

The continuity equation and motion equation of an S_2 flow surface using an arbitrary curve coordinate is [3]:

$$\frac{\partial}{\partial z^1}(r\rho W^1\sqrt{a_{22}}\sin\theta_{12}) + \frac{\partial}{\partial z^2}(r\rho W^2\sqrt{a_{11}}\sin\theta_{12}) = 0 \qquad (2)$$

$$\frac{W^2}{\sqrt{a_{22}}}\left(\frac{\partial w_2}{\partial z^1} - \frac{\partial w_1}{\partial z^2}\right) + \frac{W_\varphi}{r}\cdot\frac{\partial(V_\theta r)}{\partial z^1} = \frac{\partial I}{\partial z^1} - T\frac{\partial s}{\partial z^1} - f_1 \qquad (3)$$

---

*The direction a of a coordinate in the paper is the direction z of manuscript [2]. Except those specified, the other symbols are the same as in manuscripts [2, 3].

26

$$\frac{W_\phi}{r}\frac{\partial(V_\phi r)}{\partial x^2} - \frac{W^1}{\sqrt{a_{11}}}\left(\frac{\partial w_2}{\partial x^1} - \frac{\partial w_1}{\partial x^2}\right) = \frac{\partial I}{\partial x^2} - T\frac{\partial s}{\partial x^2} - f_2 \qquad (4)$$

$$\frac{d(V_\phi r)}{dt} = \frac{W^1}{\sqrt{a_{11}}}\frac{\partial(V_\phi r)}{\partial x^1} + \frac{W^2}{\sqrt{a_{22}}}\frac{\partial(V_\phi r)}{\partial x^2} = f_\phi = F_\phi r \qquad (5)$$

For perpendicular intersection (y, z, ϕ) coordinate system used in Fig. 1, there are

$$\sqrt{a_{11}} = \sqrt{a_{22}} = 1, \quad \theta_{12} = 90°, \quad W^1 = w_1 = W_y,$$
$$W^2 = w_2 = W_z, \quad f_1 = F_y, \quad f_2 = F_z,$$

and $$\quad \because \quad I = h + [(W)^2 - (\omega r)^2]/2, \quad B = r/r, \quad Tds = dh - dp/\rho$$

After using the various relationship equations as above, the continuity equation and motion equation are, respectively:

$$\frac{\partial(rW_y)}{r\partial y} + \frac{\partial(rW_z)}{r\partial z} + \frac{1}{\rho}\frac{d\rho}{dt} + \frac{1}{B}\frac{dB}{dt} = 0 \qquad (2')$$

$$-W_z\frac{\partial W_y}{\partial z} - W_y\frac{\partial W_y}{\partial y} + \frac{V_\phi^2}{r}\frac{\partial r}{\partial y} = \frac{1}{\rho}\frac{\partial p}{\partial y} - F_y \qquad (3')$$

$$-W_y\frac{\partial W_z}{\partial y} - W_z\frac{\partial W_z}{\partial z} + \frac{V_\phi^2}{r}\frac{\partial r}{\partial z} = \frac{1}{\rho}\frac{\partial p}{\partial z} - F_z \qquad (4')$$

$$\frac{d(V_\phi r)}{dt} = W_y\frac{\partial(V_\phi r)}{\partial y} + W_z\frac{\partial(V_\phi r)}{\partial z} = F_\phi r \qquad (5')$$

In equations, $$F = -\frac{1}{N_\phi r}\frac{1}{\rho}\frac{\partial p}{\partial\phi}\, n \qquad (6)$$

Using $p = \rho RT$ and $W_y = W_z \tan\delta$, we derive from eq. (2') and eq. (4'):

$$(1 - M_z^2)\frac{\partial W_z}{\partial z} = -(1 - M_z^2)\tan\delta\frac{\partial W_z}{\partial y} - \frac{W_z}{\rho a^2}\tan\delta\frac{\partial p}{\partial y}$$
$$+ \frac{1}{c_\phi}\frac{ds}{dt} - W_z\frac{\partial\tan\delta}{\partial y} - \left(1 + \frac{V_\phi^2}{a^2}\right)\frac{W_z}{r}\frac{\partial r}{\partial z}$$
$$- \frac{W_z}{r}\tan\delta\frac{\partial r}{\partial y} - \frac{W_z}{a^2}F_z - \frac{1}{B}\frac{dB}{dt} \qquad (7)$$
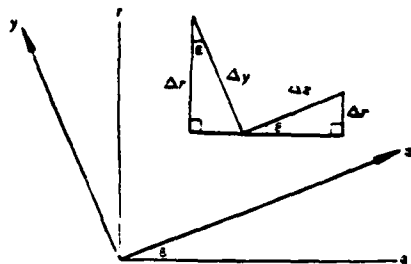
27

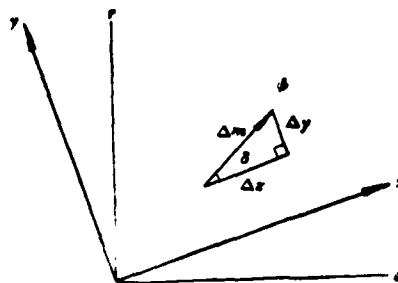Fig. 2. Concerning $\partial r/\partial y$ and $\partial r/\partial z$.

Fig. 3. Concerning $\partial y/\partial m$ and $\partial z/\partial m$.

We know from Fig. 2: $\partial r/\partial z = \sin \varepsilon$, $\partial r/\partial y = \cos \varepsilon$,

We know from Fig. 3: $\partial y/\partial m = \sin \delta$, $\partial z/\partial m = \cos \delta$,

Besides,

$$\frac{\partial \tan \delta}{\partial m} = \frac{\partial \tan \delta}{\partial y}\frac{\partial y}{\partial m} + \frac{\partial \tan \delta}{\partial z}\frac{\partial z}{\partial m}$$

By using the equations above, we obtain

$$\tan \delta \frac{\partial \tan \delta}{\partial y} + \frac{\partial \tan \delta}{\partial z} = \left(\frac{d^2 y}{d z^2}\right)_* \tag{8}$$

We substitute eq. (7) into eq. (3') and use the above equation (eq. (8)); we obtain

$$\frac{1}{\rho}\frac{\partial p}{\partial y} = -\frac{W_s^2}{1 - M_m^2}\left\{(1 - M_s^2)\left(\frac{d^2 y}{d z^2}\right)_* - \frac{\tan \delta}{r}(\sin \varepsilon + \tan \delta \cos \varepsilon)\right.$$
$$\left. -\frac{1}{2}\frac{\partial \tan^2 \delta}{\partial y} - \frac{\tan \delta}{B W_s}\frac{dB}{ds}\right\} + \frac{V_\phi^2}{r(1 - M_m^2)}[(1 - M_s^2)\cos \varepsilon + M_s^2 \tan \delta \sin \varepsilon]$$
$$-\frac{W_s \tan \delta}{1 - M_m^2}\frac{1}{c_\rho}\frac{ds}{ds} + \frac{1}{1 - M_m^2}[(1 - M_s^2)F_y + M_s^2 \tan \delta F_s] \tag{9}$$

Equation (9) is the principal equation we require.

If we let

$$\tan \lambda_y = F_y/F_\phi, \quad \tan \mu_s = F_s/F_\phi$$

28

and use eq. (5), we obtain $F_y = \tan\lambda_y \cdot d(V_\theta r)/r\,dt$, $F_z = \tan\mu_z \cdot d(V_\theta r)/r\,dt$,

Substituting the above equation into eq. (9), we obtain:

$$\frac{1}{\rho}\frac{\partial p}{\partial y} = -\frac{W_s^2}{1-M_m^2}\left\{(1-M_s^2)\left(\frac{d^2y}{dz^2}\right)_\phi - \frac{\tan\delta}{r}(\sin\varepsilon + \tan\delta\cos\varepsilon)\right.$$

$$\left. -\frac{1}{2}\frac{\partial\tan^2\delta}{\partial y} - \frac{\tan\delta}{BW_s}\frac{dB}{dt}\right\} + \frac{V_\theta^2}{r(1-M_m^2)}[(1-M_s^2)\cos\varepsilon + M_s^2\tan\delta\sin\varepsilon]$$

$$-\frac{W_s\tan\delta}{1-M_m^2}\cdot\frac{1}{c_p}\frac{ds}{dt} + \frac{1}{1-M_m^2}[(1-M_s^2)\tan\lambda_y + M_s^2\tan\delta\tan\mu_z]\frac{d(V_\theta r)}{r\,dt} \quad (9')$$

For the computation station in the gap of a blade array, there are

$$dB/dt = 0 \text{ and } d(V_{\theta r})/dt = 0$$

After substituting the above equation into eq. (9), we obtain

$$\frac{1}{\rho}\frac{\partial p}{\partial y} = -\frac{W_s^2}{1-M_m^2}\left\{(1-M_s^2)\left(\frac{d^2y}{dz^2}\right)_\phi - \frac{\tan\delta}{r}(\sin\varepsilon + \tan\delta\cos\varepsilon)\right.$$

$$\left. -\frac{1}{2}\frac{\partial\tan^2\delta}{\partial y}\right\} + \frac{V_\theta^2}{r(1-M_m^2)}[(1-M_s^2)\cos\varepsilon + M_s^2\tan\delta\sin\varepsilon]$$

$$-\frac{W_s\tan\delta}{1-M_m^2}\frac{1}{c_p}\frac{ds}{dt} \quad (10)$$

Neglecting the last term of eq. (10), this is eq. (1). We know from this that the equation used by Heterington is correct.

TRANSFORMATION OF Y DIRECTION MOTION EQUATION

Through transformation of eq. (9), we can obtain eq. (11) of [2]. This explains that the difference in form between the two is due to different coordinate systems. Actually, these two are in complete agreement.

We know from Fig. 1: $\delta = \sigma - \varepsilon$ (11)

$\varepsilon = \theta - 90°$ (12)

Besides, $M_s = M_s\cos\delta/\cos\sigma$ (13)

$\left(\frac{d^2y}{dz^2}\right)_\phi = \frac{\cos^3\sigma}{\cos^3\delta}\left(\frac{d^2r}{dz^2}\right)_\phi$ (14)

29
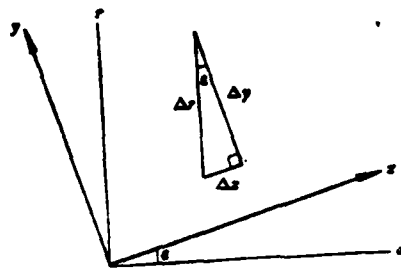
Fig. 4.   Concerning ∂y/∂r and ∂z/∂r.

From Fig. 4,

$$\partial y/\partial r = \cos\varepsilon, \quad \partial z/\partial r = \sin\varepsilon,$$

and

$$\frac{\partial q}{\partial r} = \frac{\partial q}{\partial y}\cos\varepsilon + \frac{\partial q}{\partial z}\sin\varepsilon,$$

$$\frac{\partial q}{\partial m} = \frac{\partial q}{\partial y}\sin\delta + \frac{\partial q}{\partial z}\cos\delta,$$

Therefore

$$\frac{\partial \tan\sigma}{\partial r} = \frac{\sin\varepsilon}{\cos\delta}\frac{\partial \tan\sigma}{\partial m} + \frac{\cos\sigma}{\cos\delta}\frac{\partial \tan\sigma}{\partial y}$$

Considering

$$\frac{\partial \tan\sigma}{\partial m} = \cos\sigma\left(\frac{d^2r}{d\sigma^2}\right)_* \qquad \text{and} \quad \partial\varepsilon/\partial y = 0$$

We obtain

$$\frac{\partial \tan\sigma}{\partial y} = \frac{\cos^2\delta}{\cos^2\sigma}\frac{\partial \tan\delta}{\partial y}$$

Substituting the above equation into the expression equation of ∂tanσ/∂r, we obtain the following equation after putting into order:

$$\frac{\partial \tan\delta}{\partial y} = \frac{\cos\sigma}{\cos\delta}\frac{\partial \tan\sigma}{\partial r} - \sin\varepsilon\frac{\cos^2\sigma}{\cos^2\delta}\left(\frac{d^2r}{d\sigma^2}\right)_* \qquad (15)$$

30

For the blade force:

$$F_y = F_r \cos\varepsilon - F_\varepsilon \sin\varepsilon \qquad (16)$$

$$F_\varepsilon = F_r \sin\varepsilon + F_\varepsilon \cos\varepsilon \qquad (17)$$

If we let $\tan\lambda = F_r/F_\varphi, \tan\mu = F_\omega/F_\varphi,$

By using eq. (5), we obtain:

$$F_r = \tan\lambda \cdot d(V_\theta r)/(r\, d\varepsilon) \qquad (18)$$

$$F_\varepsilon = \tan\mu \cdot d(V_\theta r)/(r\, d\varepsilon) \qquad (19)$$

Substituting eqs. (11) through (19) into eq. (9), we obtain eq. (11) of [2]. Hence, eq. (9) is in agreement with eq. (11) of [2].

LITERATURE

1. Wu Zhonghua, On Simplifying Radial Equilibrium, Axial Symmetric Flow, Flow Through Stream Calculation, Three-dimensional Theory of S_1 and S_2 Relative Flow Surfaces, and Computer Program, Institute of China Science and Technology Information, 1974.

2. Hong Hejing, Aerodynamic Calculation of Flow of S_2 Stream Surface Using a Non-radial Calculation Station in Blade Passage of Turbomachines, Kexue Tongbao [Science Journal], 22, 7 (1977).

3. Wu Zhonghua, Three Dimensional Flow Fundamental Equation and Solution Method of Turbomachines Using Non-perpendicular Intersection Curve Coordinates and Non-perpendicular Intersection Velocity Component, Jixie Gongcheng Xuebao [Journal of Mechanical Engineering], 15, 1 (1979).

APPENDIX   DERIVATION OF TRANSFORMATION OF EQ. (9) INTO EQ. (11) of [2]

We obtain from eqs. (11) through (13),

$$\sin\varepsilon + \tan\delta\cos\varepsilon = \sin\sigma/\cos\delta \qquad (A\text{-}1)$$

$$(1 - M_t^2)\cos\varepsilon + M_t^2 \tan\delta\sin\varepsilon = (1 - M_t^2)\cos\varepsilon - M_t^2 \tan\sigma\sin\varepsilon \qquad (A\text{-}2)$$

$$M_t^2 \tan\delta\cos\varepsilon - (1 - M_t^2)\sin\varepsilon = M_t^2 \tan\sigma\cos\varepsilon + (\tan^2\sigma M_t^2 - 1)\sin\varepsilon \qquad (A\text{-}3)$$

Substituting eqs. (14)-(17), (A-1), (A-2) and (A-3) into eq. (9), we obtain after ordering:

31

$$\frac{1}{\rho}\frac{\partial p}{\partial y} = -\frac{W_s^2}{1-M_m^2}\left\{\left[(1-M_s^2)\frac{\cos^2\sigma}{\cos^2\delta} + \tan\delta\sin s\frac{\cos^2\sigma}{\cos^2\delta}\right]\left(\frac{d^2r}{ds^2}\right)_s\right.$$
$$-\left(\frac{\sin\sigma}{\cos\delta}\frac{\tan\delta}{r} + \tan\delta\frac{\cos\sigma}{\cos\delta}\frac{\partial\tan\sigma}{\partial r}\right) - \frac{\tan\delta}{BW_s}\frac{dB}{ds}\right\}$$
$$+\frac{V_\theta^2}{r(1-M_m^2)}\left[(1-M_s^2)\cos s - M_s^2\tan\sigma\sin s\right] + \frac{s_1}{1-M_m^2}\left\{[(1-M_s^2)\cos s\right.$$
$$\left.- M_s^2\tan\sigma\sin s]F_r + [M_s^2\tan\sigma\cos s + (\tan^2\sigma M_s^2 - 1)\sin s]F_s\right\}$$
$$-\frac{W_s\tan\delta}{1-M_m^2}\frac{1}{c_p}\frac{ds}{dt} \tag{A-4}$$

And ∴

$$(1-M_s^2)\cos^2\sigma/\cos^2\delta + \tan\delta\sin s\cos^2\sigma/\cos^2\delta$$
$$= [(1-M_s^2)\cos s - M_s^2\tan\sigma\sin s]\cos^2\sigma/\cos^2\delta \tag{A-5}$$

$$\frac{\sin\sigma}{\cos\delta}\frac{\tan\delta}{r} + \tan\delta\frac{\cos\sigma}{\cos\delta}\frac{\partial\tan\sigma}{\partial r} = \frac{\cos^2\sigma}{\cos^2\delta}(\tan\sigma\cos s - \sin s)\left(\frac{\tan\sigma}{r} + \frac{\partial\tan\sigma}{\partial r}\right) \tag{A-6}$$

$$V_\theta^2 = W_s^2\tan^2\alpha \tag{A-7}$$

Substituting eqs. (A-5) to (A-7) into eq. (A-4) and considering eqs. (11), (12), (18) and (19), we obtain

$$\frac{1}{\rho}\frac{\partial p}{\partial y} = \frac{W_s^2}{1-M_m^2}\left\{(\tan\sigma\sin\theta + \cos\theta)\left(\frac{\tan\sigma}{r} + \frac{\partial\tan\sigma}{\partial r} + \frac{1}{B}\frac{dB}{ds} - \frac{1}{c_p}\frac{ds}{ds}\right)\right.$$
$$+ [(1-M_s^2)\sin\theta + M_s^2\tan\sigma\cos\theta]\left[\frac{\tan^2\alpha}{r} - \left(\frac{d^2r}{ds^2}\right)_s + \frac{\tan\lambda}{W_s'r}\frac{d(V_\theta r)}{ds}\right]$$
$$\left.+ [M_s^2\tan\sigma\sin\theta + (1-M_s^2\tan^2\sigma)\cos\theta]\frac{\tan\mu}{W_s'r}\frac{d(V_\theta r)}{ds}\right\} \tag{A-8}$$

Neglecting the term ds/da in eq. (A-8) and considering

$$\left(\frac{d^2r}{ds^2}\right)_s = \left(\frac{d\tan\sigma}{ds}\right)_s$$

We obtain eq. (11) of [2]. Therefore, these two equations are in complete agreement.

32

NUMERICAL CALCULATION OF SUBSONIC COMPRESSIBLE TURBULENT FLOW IN A CONICAL DIFFUSER*

Gao Lijun, Wu Wendong, and Wang Yingshi
Institute of Engineering Thermophysics, Chinese Academy of Sciences

In this paper, vorticity ω and stream function Ψ are used as dependent variables to predict the turbulent flow. Generally. the method can be used to calculate both recirculating flow and non-recirculating flow. The calculation of the turbulent flow in a conical diffuser having a total divergence angle of 10°, and with ununiform velocity distribution at entry is carried out, Because the flow relates only to the developing process of turbulence boundary layer, Prandte mixing length hypothesis is used in this calculation.

The numerical results agree with the experimental data[a] quite well. It shows that this method can be applied to the design of diffuser without recirculating flow.

I. FOREWORD

For more than ten years, the numerical calculation method was applied in the flow process of a diffuser because of rapid development of calculation fluid mechanics. The paper tries to begin from an elliptical model equation to solve for the viscous flow problem in a diffuser. Theoretically, this approach can be adapted to solve for a flow situation with or without

---

33

recirculating flow. As the first step, the authors calculate the flow of a small expansion angle diffuser. Since the flow is a development process of a turbulent flow boundary layer, the calculation of the turbulent flow viscosity coefficient can use the Prandtl mixing length hypothesis. The expansion angle of the diffuser is 10°, and the data used for comparison are taken from manuscript [4]. The calculation result and experimental data are in good agreement.

II. FUNDAMENTAL EQUATIONS

The authors use the spherical coordinate system (ξ_1=R, ξ_2=β, and ξ_2=θ), referring to Fig. 1. The fundamental equation set is established by focusing on stability, axial symmetry and two dimensional flow. In addition, assumptions include that the ideal gas, and C_p and λ are constants.
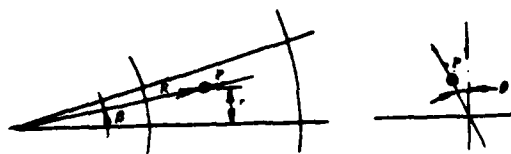
Fig. 1

The continuity equation:
$$\partial(R r G_1)/\partial R + \partial(r G_2)/\partial \beta = 0 \tag{1}$$
G_1 and G_2 are components of G=ρV.

The momentum equation:

ξ_1: $\operatorname{div}(G V_1 - T_1) - (\rho V_2^2 - T_{2,2})/R + (T_{2,2}/r)\sin\beta + \partial p/\partial R = 0$ (2)

ξ_2: $\operatorname{div}[R(G V_2 - T_2)] - (T_{3,2}/r)\cos\beta - (G_2 V_2 - T_{2,2}) \cdot (\partial R/\partial \beta)/R^2$
  $+ (\partial p/\partial \beta)/R = 0$ (3)

In order to avoid the difficulty of determining the pressure boundary conditions, vorticity ω is introduced in the calculation, and the pressure terms in eqs. (2) and (3) are cancelled, in deriving the momentum eq. [1] with ω as the variable.   34

$$r^2\{\partial[(\omega/r)\cdot(\partial\psi/\partial\beta)]/\partial R - \partial[(\omega/r)\cdot(\partial\psi/\partial R)]/\partial\beta\}$$
$$- \partial\{Rr^3\partial[\mu_{eff}(\omega/r)]/\partial R\}/\partial R - \partial\{(r^3/R)\cdot\partial[\mu_{eff}(\omega/r)]/\partial\beta\}/\partial\beta$$
$$- r^2\{\partial[(V_1^2 + V_2^2)/2]/\partial R\}(\partial\rho/\partial\beta)$$
$$+ r^2\{\partial[(V_1^2 + V_2^2)/2]/\partial\beta\}(\partial\rho/\partial R) = 0 \tag{4}$$

The flow function equation:

$$\partial\{[R/(\rho r)](\partial\psi/\partial R)\}/\partial R + \partial\{[1/(\rho Rr)](\partial\psi/\partial\beta)\}/\partial\beta + R\omega = 0 \tag{5}$$

The energy equation:

$$\partial(h^*\partial\psi/\partial\beta)/\partial R - \partial(h^*\partial\psi/\partial R)/\partial\beta - \partial(\Gamma_{h,eff}Rr\partial h^*/\partial R)/\partial R$$
$$- \partial[\Gamma_{h,eff}(r/R)\partial h^*/\partial\beta]/\partial\beta - \partial[\mu_{eff}Rr(1 - 1/\sigma_{h,eff})\partial(V^2/2)/\partial R]/\partial R$$
$$- \partial\{[\mu_{eff}(r/R)\cdot(1 - 1/\sigma_{h,eff})]\partial(V^2/2)/\partial\beta\}/\partial\beta = 0 \tag{6}$$

In eq. (6), h^* is the total enthalpy; $\sigma_{h,eff}$ is the effective Prandtl number of the turbulent flow; $\Gamma_{h,eff}$ is the effective heat exchange coefficient of the turbulent flow; and $\Gamma_{h,eff} = \mu_{eff}/\sigma_{h,eff}$, μ_{eff} is the effective viscosity coefficient of the turbulent flow.

From eqs. (4) to (6), the general form of the fundamental equation can be derived:

$$a_\phi[\partial(\phi\partial\psi/\partial\beta)/\partial R - \partial(\phi\partial\psi/\partial R)/\partial\beta] - \partial[b_\phi Rr\partial(c_\phi\phi)/\partial R]/\partial R$$
$$- \partial[b_\phi(r/R)\partial(c_\phi\phi)/\partial\beta]/\partial\beta + Rrd_\phi = 0 \tag{7}$$

Corresponding to different coefficients a_ϕ, b_ϕ, c_ϕ, and d_ϕ of different variables ϕ, the following table shows the contents:

ϕ	a_ϕ	b_ϕ	c_ϕ	d_ϕ
ω/r	r^2	r^4	μ_{eff}	$-(r/R)\{(\partial\rho/\partial\beta)\partial[(V_1^2 + V_2^2)/2]/\partial R - (\partial\rho/\partial R)\partial[(V_1^2 + V_2^2)/2]/\partial\beta\}$
ψ	0	$1/(\rho r^2)$	1	$-\omega/r$
h^*	1	$\Gamma_{h,eff}$	1	$-(1/R)\partial[\mu_{eff}Rr(1 - 1/\sigma_{h,eff})\partial(V^2/2)/\partial R]/\partial R$ $-(1/Rr)\partial[\mu_{eff}(r/R)(1 - 1/\sigma_{h,eff})\partial(V^2/2)/\partial\beta]/\partial\beta$

For solving variables ω/r, ψ and h^*, the calculation of the related physical quantities is as follows:

35

Velocity: $\quad V_1 = (\partial\psi/\partial\beta)/(\rho R r), \quad V_2 = -(\partial\psi/\partial R)/(\rho r)$ (8)

Pressure: Calculation of pressure is based on the momentum equations (2) and (3); the calculation of the relative viscosity stress in eqs. (2) and (3) is as follows:

$$T_{1,1} = \mu_{eff}[2\partial V_1/\partial R - (2/3)\mathrm{div}\,V]$$ (9)

$$T_{2,2} = \mu_{eff}[2(\partial V_2/\partial\beta)/R + 2V_1/R - (2/3)\mathrm{div}\,V]$$ (10)

$$T_{3,3} = \mu_{eff}[2(V_1\sin\beta + V_2\cos\beta)/r - (2/3)\mathrm{div}\,V]$$ (11)

$$T_{1,2} = T_{2,1} = \mu_{eff}[(\partial V_1/\partial\beta)/R + R\partial(V_2/R)/\partial R]$$ (12)

In the equations,

$$\mathrm{div}\,V = 1/(Rr)[Rr\partial V_1/\partial R + V_1 R\sin\beta + V_1 r + r\partial V_2/\partial\beta + V_2 R\cos\beta]$$ (13)

We substitute eqs (9) to (13) into the momentum equations (2) and (3); $\partial p/\partial R$ and $\partial p/\partial\beta$ can be derived with values shown in the following:

$$\begin{aligned}
\partial p/\partial R = & -(1/Rr)\partial\{Rr[\rho V_1^2 - 2\mu_{eff}\partial V_1/\partial R + (2/3)\mu_{eff}\,\mathrm{div}\,V]\}/\partial R \\
& - (1/Rr)\{\partial[r\rho V_2 V_1 - r\mu_{eff}(\partial V_1/\partial\beta)/R - r\mu_{eff}(\partial V_2/\partial R \\
& - V_2/R)]/\partial\beta\} + [\rho V_2^2 - 2\mu_{eff}(\partial V_2/\partial\beta)/R \\
& - 2\mu_{eff}V_1/R + (2/3)\mu_{eff}\mathrm{div}\,V]/R \\
& - [2\mu_{eff}(V_1\sin\beta + V_2\cos\beta)/r \\
& - (2/3)\mu_{eff}\,\mathrm{div}\,V]/R
\end{aligned}$$ (14)

$$\begin{aligned}
\partial p/\partial\beta = & [1/(Rr)]\partial\{R^2 r[\mu_{eff}(\partial V_2/\partial R - V_2/R) + \mu_{eff}(\partial V_1/\partial\beta)/R] \\
& - \rho R^2 r V_1 V_2\}/\partial R + [1/(Rr)]\partial\{Rr[\mu_{eff}(2/R)\partial V_2/\partial\beta \\
& + 2\mu_{eff}V_1/R - (2/3)\mu_{eff}\,\mathrm{div}\,V - \rho V_2^2]\}/\partial\beta \\
& - \mu_{eff}[2(V_1\sin\beta + V_2\cos\beta)/r \\
& - (2/3)\mathrm{div}\,V]/\tan\beta
\end{aligned}$$ (15)

$$p_B = p_A + 0.5[(\partial p/\partial R)_A + (\partial p/\partial R)_B](R_B - R_A)$$ (16)

or $\quad p_C = p_D + 0.5[(\partial p/\partial\beta)_C + (\partial p/\partial\beta)_D](\beta_C - \beta_D)$ (17)

Density: $\quad \rho = p/gRT$ (18)

In the equation, $\quad T = (h^* - V^2/2g)/c_p$ (19)

Effective viscosity coefficient of turbulent flow: $\mu_{eff} = \mu_L + \mu_T$ (20)

36

μ_L is the viscosity coefficient of the laminar flow; and μ_T is the viscosity coefficient of the turbulent flow. The calculation of μ_T adopts the Prandtl mixing length hypothesis; i.e., $\mu_T = \rho l_m^2 |\partial V_1/\partial y|$.

The calculation of mixing length l_m is based on Escudier's empirical formula (5).

When $y/\delta \leqslant \lambda/k$,

$$l_m/\delta = Ry/\delta \qquad (21)$$

When $y/\delta > \lambda/k$,

$$l_m/\delta = \lambda \qquad (22)$$

In the equations, k=0.41 and λ=0.09.

In the two above equations, y is the vertical distance from the cone surface of the diffuser; δ is the boundary layer thickness. In the calculation, $V_1/V_{max} \geqslant 0.99$ is used to determine δ. From eqs. (21) and (22), it is apparent that there is a certain limitation in using the Prandtl mixing length hypothesis. When $|\partial V_1/\partial y| \to 0$,

μ_T seems to have the tendency of approaching zero; of course, this is not consistent with the physical significance, so this is treated in calculation [2]. When $|\partial V_1/\partial y|$ is smaller than a certain small quantity (corresponding to $V_1/V_{max} \geqslant 0.99$) and if we let $\mu_T = \rho l_m (l_m |\partial V_1/\partial y|)$.

In the equation, $l_m |\partial V_1/\partial y| = 0.01(V_{1,j} + V_{1,j+1})/2$,

j and j+1 indicate two adjacent nodal points along the ξ_2 direction.

III. BOUNDARY CONDITIONS

Inlet: $\omega/r = (R_0 \partial V_2/\partial R - \partial V_{1,0}/\partial \beta)/(R_0^2 \sin \beta)$. The lower angle 0 indicates the inlet.

$$\Psi = R_0^2 \rho_0 \int_0^{\beta_1} V_{1,0}(\beta) \sin \beta d\beta,$$

$V_{1,0}$ is the non-uniform distribution; taken from [4], $V_{2,0}$=0.

$$h^* = c_p T_0 + V_{1,0}^2/2g,$$

293K is taken for T_0.

Upper wall surface: $(\omega/r)_N = - [3(\Psi_{N-1} - \Psi_N)/(\rho r_N^2 R^2 \beta_{N-1}^2) + 0.5(\omega/r)_{N-1}]$.

The lower angles N and N-1 indicate the nodal points on the wall surface, and the nodal point of a mesh lattice separating from the wall surface.

$$\Psi = R_0^2 \rho_0 \int_0^{\beta_N} V_{1,0}(\beta) \sin(\beta) d\beta$$

$$\partial h^*/\partial y - (V_2 \partial V_1/\partial y)/g = 0,$$

y is the vertical distance from the wall surface.

37

The central line: $\omega/r = -8[(\Psi_3 - \Psi_1)/\beta_3^2 - (\Psi_2 - \Psi_1)/\beta_2^2]/[\rho R^4(\beta_3^2 - \beta_2^2)]$.

The lower angles 1, 2 and 3 indicate the central line and the adjacent nodal points, referring to Fig. 2. $\quad \Psi = 0; \quad \partial h^*/\partial \beta = 0$.

Outlet: $\qquad \partial(\omega/r)/\partial R = \partial \Psi/\partial R = \partial h^*/\partial R = 0$

Fig. 2.
Key: (*) Central line.
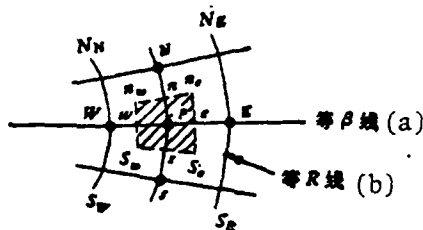
Fig. 3.
Key: (a) Line of equal β; (b) Curve of equal R.

IV. ESTABLISHING AND SOLVING FOR DIFFERENCE EQUATIONS

Derived from eq. (7), the difference equation solving for numerical calculation should be able to plot a series of mutually perpendicular lines of equal R and lines of equal β along directions of R and β. We integrate the control area enveloping the point P (the portion of cross sectional lines in Fig. 3). In addition, in the convection term integration, the average variables are taken as the up-wind value in deriving the following difference equation [1]:

$$\phi_P = \frac{\sum\limits_{i=N,S,E,W} \{[A_i' + c_{\phi,i}(b_{\phi,i} + b_{\phi,P})B_i']\phi_i\} - d_{\phi,P}}{\sum\limits_{i=N,S,E,W} \{A_i' + c_{\phi,P}(b_{\phi,i} + b_{\phi,P})B_i'\}} \qquad (23)$$

In the equation,

$$A_i' = A_i/V_P, \quad B_i' = B_i/[V_P(b_{2,i} + b_{2,P})];$$
$$A_E = (a_{\phi,P}/8)[(\Psi_{SE} + \Psi_S - \Psi_{NE} - \Psi_N) + |\Psi_{SE} + \Psi_S - \Psi_{NE} - \Psi_N|]$$
$$A_W = (a_{\phi,P}/8)[(\Psi_{NW} + \Psi_N - \Psi_{SW} - \Psi_S) + |\Psi_{NW} + \Psi_N - \Psi_{SW} - \Psi_S|]$$

38

$$A_S = (a_{\phi,P}/8)[(\Psi_{SE} + \Psi_W - \Psi_{SE} - \Psi_s) + |\Psi_{SW} + \Psi_W - \Psi_{SE} - \Psi_E|]$$

$$A_N = (a_{\phi,P}/8)[(\Psi_{NE} + \Psi_E - \Psi_{NW} - \Psi_W) + |\Psi_{NE} + \Psi_E - \Psi_{NW} - \Psi_W|]$$

$$B_E = R_P(b_{\phi,E} + b_{\phi,P})(\beta_N - \beta_S)(R_E + R_P)\sin\beta_P/[8(R_E - R_P)]$$

$$B_W = R_P(b_{\phi,W} + b_{\phi,P})(\beta_N - \beta_S)(R_W + R_P)\sin\beta_P/[8(R_P - R_W)]$$

$$B_N = (b_{\phi,N} + b_{\phi,P})(R_E - R_W)(\sin\beta_N + \sin\beta_P)/[8(\beta_N - \beta_P)]$$

$$B_S = (b_{\phi,S} + b_{\phi,P})(R_E - R_W)(\sin\beta_S + \sin\beta_P)/[8(\beta_P - \beta_S)]$$

$$V_P = R_P^2\sin\beta_P(R_E - R_W)(\beta_N - \beta_S)/4$$

For convenience of convergence, the implicit iterated substitution formula is taken for the ω/r value on N-1 points.

$$(\omega/r)_{N-1} = \frac{\sum_{i=E,S,W}\{[A_i' + c_{\phi,i}(b_{\phi,i} + b_{\phi,N-1})B_i']\phi_i\} + \{\quad\}_N C_1 - d_{\phi,N-1}}{\sum_{j=N,S,E,W}\{A_j' + c_{\phi,N-1}(b_{\phi,j} + b_{\phi,N-1})B_j'\} - \{\quad\}_N C_2}, \quad (24)$$

ϕ represents the corresponding ω/r.

$$\{\quad\}_N = \{A_N' + c_{\phi,N}(b_{\phi,N} + b_{\phi,P})B_N'\}$$
$$C_1 = -3(\Psi_{N-1} - \Psi_N)/(r_{N-1}^2 n_{N-1}^2 \rho_{N-1}), \quad n_{N-1} = R(\beta_N - \beta_{N-1})$$
$$C_2 = -1/2$$

Selections of mesh lattices are as follows:

ξ_1: equidistant mesh lattice with lattice distance of 0.02 meter.

ξ_2: unequal mesh lattice. For viscous flow, since a development process exists in the boundary layer, the velocity variation is greater within the boundary layer, so the mesh lattices should be denser. The mesh lattices which are wider apart will cause inaccurate calculation results.

Figure 5 indicates the influence on the central velocity of
$[\epsilon = (\beta_{i+1} - \beta_i)/(\beta_i - \beta_{i-1}) = 0.9, 0.943, 1]$ for selecting different values of ϵ. Compared to the experimental values, the error is the smallest when $\epsilon = 0.9$. Therefore, the calculation proceeds with $\epsilon = 0.9$.

39

In this calculation, the superrelaxation method is used for solution; the superrelaxation factors are: $\alpha_{u,r} = 1$, $\alpha_{u} = 1.15$, $\alpha_{h^*} = 1$ Calculating for convergence on all internal points satisfying $[(\phi^n - \phi^{n-1})/\phi^n]_{max} \leq \lambda$

The value of λ is 0.0005; n represents the number of repetitions at this time; and (n-1) represents the number of repetitions for the last time.

V. CALCULATION RESULTS AND ANALYSIS

This calculation is conducted on a straight wall conical diffuser with divergence angle of 10°, inlet radius of 0.07762 meter, and length of 0.2 meter, proceeding under the condition of uneven velocity at the inlet. The calculation results are as follows:

Figure 4 indicates the variation of the static pressure restoration coefficient $\bar{C}_p = (p_i - p_0)/(0.5\rho_0 V_{1,0,m}^2)$ with R. The static pressure is the arithmetic mean of pressures at various points of the cross sectional surface. $V_{1,0,m}$ indicates the fringe velocity at the boundary layer of the inlet along the ξ_1 direction.

Figure 5 indicates the situation that the velocity at the fringe of the boundary layer reduces with increase in diffuser length. Compared to the experimental data in [4], this is relatively satisfactory.

Figure 6 indicates the influence on value δ/R_0 of two inlet velocities (uniform and non-uniform). The calculation is conducted in the situation that the inlet volumetric flow is under the same conditions. The inlet non-uniform velocity distribution (Fig. 7) is derived using the method provided by [3] with the fringe velocity of the boundary layer as provided by [4]. From Fig. 6, it is apparent that the difference is relatively high when induced by two different inlet velocities.

Figure 9 indicates the situation when the turbulent flow viscosity coefficient at a certain cross sectional surface varies with β. In the diagram, values of points A, B and C are apparently irrational; this is

caused by using the Prandtl mixing length model. However, from the calculation result, there is no undesirable influence on the velocity distribution (Fig. 8).
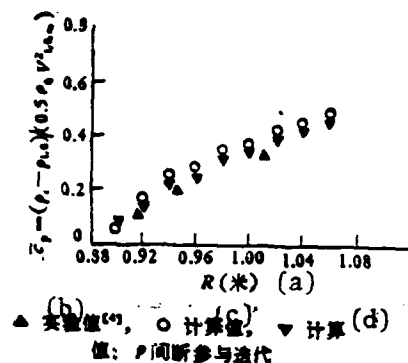
Fig. 4.
Key: (a) Meter; (b) Experimental value; (c) Calculation value; (d) Calculation value; (e) p takes part in repetitive substitutions intermittently.
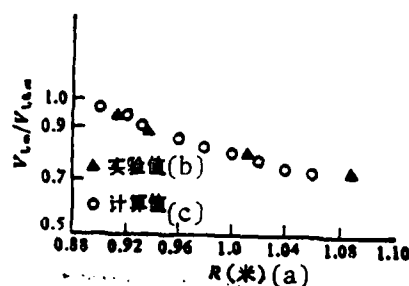
Fig. 5.
Key: (a) Meter; (b) Experimental value; (c) Calculation value.
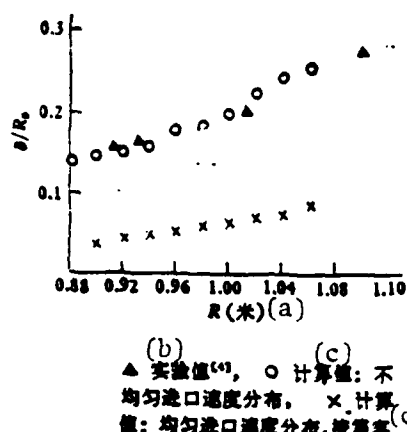
Fig. 6.
Key: (a) Meter; (b) Experimental value; (c) Calculation value: velocity distribution of nonuniform inlet velocity; (d) Calculation value: distribution of uniform inlet velocity, distributed according to equal volume flow.
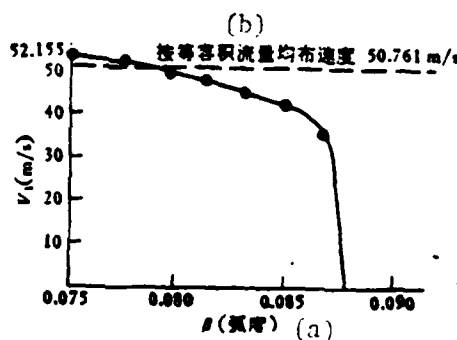
Fig. 7.
Key: (a) Radian; (b) Velocity of equal volume flow uniformly distributed.

VI. CONCLUSIONS

(1) If we compare the calculation results using this method and that of the experimental results, the degree of agreement is good.
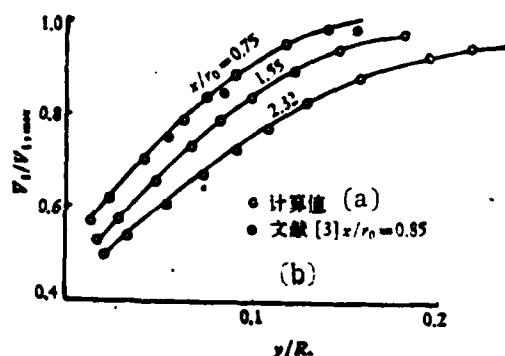
Fig. 8.
Key: (a) Calculated value; (b)
Manuscript.
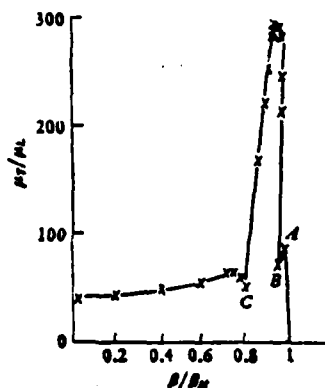
Fig. 9.

(2) The calculation proves the important influence on flow field of the
inlet velocity distribution. The calculation results are obviously different
using uniform and nonuniform inlet velocity distributions on the same diffuser.

(3) This program can be used to calculate the flow in a small expansion
angle diffuser of the same category flow without separation. As the compressi-
bility influence is counted, this program can be used for calculation of
subsonic flow of a wider range of inlet M number.

(4) To shorten the calculation time, in addition to the adoption of
better relaxation factors, the pressure subprogram can intermittently take
part in repetitive substitutions. Thus, the accuracy of calculation results
is not affected, referring to Fig. 4.

LITERATURE

[1] A. D. Gosman., et al.: Heat and Mass Transfer in Recirculating Flow. Academic Press, (1969).
[2] S. V. Patankar, D. B. Spalding: Heat and Mass Transfer in Boundary layers, International Text-
     book Company Ltd, (1970).
[3] N. E. A. Wirasinghe. R. S. Neve: The Prediction of Turbulent Boundary Layer Parameters in
     Conical Diffuser Flows, The Aeronautical Quarterly, (August 1974).
[4] Harvey, R. Fraser: The Turbulent Boundary Layer in a Conical Diffuser, Journal of The
     Hydraulics Division, (June 1958), p. 1684—1.
[5] B. E. Launder, D. B. Spalding: Mathematical Models of Turbulence. Academic Press, (1972).

THE ANALYSIS OF FORCES AND POWERS IN TURBOMACHINERY GAS DYNAMICS*

Wang Jiasheng

Shanghai Institute of Mechanical Engineering

Correctly analyse the forces and Powers are an very important problem in turbomachinery gas dynamics. This problem was discussed detaily in this paper and was concluded that the realization of forces and powers are concerned with the situation of observers. When we discuss the forces, we must point out the situation of observers; When we discuss the powers, we must point out what force to work in . what' motion.

The paper is written on the basis of the characteristics of gas motion in turbomachinery and the situation of observers; the paper stresses the discussion of acting forces and the realization of power produced.

We arbitrarily take a micro-element control body $dV = dy_1 dy_2 dy_3$ in a Cartesian coordinate system $oy_1 y_2 y_3$. It is not difficult to apply the momentum principle to derive the micro-element power dL of an acting force on micro-element system ρdV, which is

$$dL = \frac{\partial}{\partial y_i} (C_i p_{ii}) dV + \rho f_i C_i dV$$

We develop the above equation and apply a N-S equation; we can immediately derive the micro-element power of an acting force on a unit of mass of gas

$$dl = dL / \rho dV = C \cdot \frac{DC}{Dt} + \frac{1}{\rho} p_{ii} D_{ii} \qquad (1)$$

In the equation, $D_{ij} = \partial C_j / \partial y_i$ is the element of the displacement tensor.

It is apparent from eq. (1) that the micro power (acting force on a unit mass of gas) is composed of two parts: the first is the numerical product of velocity C and acceleration DC/Dt; this is not related to deformation of the gas micro-element system. This portion of the power is called the migrating power. The second is related to the stress tensor and displacement tensor; i.e., it is related to deformation of the gas micro-element system. This portion of the power is called the deformation power.

For the migrating power, since the unit mass of gas is taken, the force acting on a unit mass of gas is equivalent to acceleration of gas motion. Then, the discussion of the acting force can be substituted with discussion of acceleration.

As is well known, the realization of velocity and acceleration in turbo-machinery is related to the observer's position. Or, it is necessary to point out whether the adopted system is inertia system or not an inertia system. For convenience in discussion, we call the observer situated in an inertia system the absolute observer, while the observer situated in the non-inertia system is called the relative observer.

In the following, the realization problem of the acting force is discussed first.

(A) The problem of the acting force of a gas

(1) To an absolute observer, the observed absolute acceleration $D_a C/Dt$ can be expressed as

$$D_a C/Dt = DW/Dt + 2\omega \times W + \omega \times (\omega \times r_r) \qquad (2)$$

It is apparent from the above equation, as viewed by an absolute observer, that the force acting on a unit mass of gas include: (a) the force DW/Dt producing relative acceleration of a unit mass of gas, (b) the force $2\omega \times W$,

44

producing Geshi [transliteration] of a unit mass of gas is called the Geshi force; and (c) the force $\omega x(\omega xr_p)$ producing centripetal acceleration of a unit mass of gas is called the centripetal force.

(2) To a relative observer moving with the rotating wheel, the observer views the rotating wheel as stationary but the gas (in the rotating wheel) moves with velocity W and acceleration DW/Dt. However, the force the observer actually observes is D_aC/Dt, $D_aC/Dt \neq DW/Dt$,

that is, the force acting on a unit mass of gas is not equivalent to the acceleration thus produced. In order to understand this conflicting phenomenon, the observer assumes two other forces as he considers that the acting force should include: (a) the force D_aC/Dt directly observed by the relative and absolute observers; (b) the assumed inertia force $-\omega x(\omega xr_p)$, the so-called centrifugal force; and (c) another assumed inertia force $-2\omega xW$. In order to distinguish the force from the Geshi force in the inertia system, this force is called the Geshi inertia force. Then

$$DW/Dt = D_aC/Dt/\omega x(\omega xr_p) - 2\omega xW$$

It is apparent that while analyzing the action force in the gas dynamics of turbomachinery, it is necessary to mention the position where the observer is attempted. To an absolute observer, the Geshi force and centripetal force make sense because these forces are observed by the absolute observer as two force components of a force D_aC/Dt. To a relative observer, the Geshi inertia force and centrifugal force make sense because these two forces explain to the relative observer an assumed force under the action of a force D_aC/Dt but have an "irrational" phenomenon of producing DW/Dt acceleration.

Together with this conclusion, there necessarily exists a problem of views on producing power by two observers.

(B) The problem of producing power by gas

(1) Migrating power   From equation (1) and $C=W+\omega xr_p$, we can obtain
$C \cdot D_aC/Dt = [DW/Dt + \omega x(\omega xr_p) + 2\omega xW] \cdot (W + \omega xr_p)$.

45

The left side of the above equation can be rewritten into $(D_a/Dt)(C^2/2)$. On the right side, six terms can be obtained after development. Their individual physical significance can be discussed as follows:

(a) $$DW/Dt \cdot W = \frac{D}{Dt}\left(\frac{W^2}{2}\right)$$ indicates the power created by the

force producing the relative acceleration for the relative motion. The term is equivalent to the variation rate with time t of relative kinetic energy by a unit mass of gas.

(b) $$DW/Dt \cdot (\omega \times r_p) = \omega \frac{D(r W_\theta)}{Dt} = \frac{D(u W_\theta)}{Dt}$$ indicates the power

produced by force DW/Dt for tractive motion.

(c) $$[\omega \times (\omega \times r_p)] \cdot W = -\frac{D}{Dt}\left(\frac{u^2}{2}\right)$$ indicates the power acting on

the gas by a centripetal force in relative motion.

(d) $2(\omega \times W) \cdot W = 0$ indicates the power acting on the gas by the Geshi force in relative motion. Since the Geshi force is consistently perpendicular to the relative velocity W, the power produced is zero.

(e) $$2(\omega \times W) \cdot (\omega \times r_p) = 2 \frac{D}{Dt}\left(\frac{u^2}{2}\right)$$ indicates the power acting

on the gas by the Geshi force in tractive motion; this indicates that the Geshi force does produce power on tractive motion.

(f) $[\omega \times (\omega \times r_p)] \cdot (\omega \times r_p) = 0$ is the power produced (zero) by centripetal force on tractive power.

Similar to discussion of the acting force, to a relative observer, since $C \cdot D_a C/Dt \neq DW/Dt \cdot W$, in order to explain this "irrational" phenomenon, in the view of the relative observer, in addition to $DW/Dt \cdot W$. the virtual power should be added: $-DW/Dt \cdot (\omega \times r_p)$; $[-\omega \times (\omega \times r_p)] \cdot W$; $[-2\omega \times W] \cdot W$.

Comprehending the above analyses, we come to the view:

(a) While discussing the power created on the gas, it is necessary to make known the position the observer is in. To an absolute observer, the Geshi force and centripetal force make sense for power acting on the gas. To a relative observer, the Geshi inertia force and centrifugal force make sense.

(b) It is irrational to make the statement, "a certain force does work (not does 'no' work)" but to clarify, "a certain force does work (or does no work) on certain motion."

(2) The deformed power can use the stress tensor expression equation of equation (1) and Newtonian fluid $p_{ij} = - p\delta_{ij} + 2\mu S_{ij} - 2/3 \mu \delta_{ij} \operatorname{div} C$

rewritten into the following (in the equation δ_{ij} is the Kronecker sign and S_{ij} is the deformation tensor element):

$$(1/\rho)p_{ij}D_{ij} = (1/\rho)(- p\delta_{ij} + 2\mu S_{ij} - 2/3\mu\delta_{ij}\operatorname{div} C)D_{ij}$$

From $\quad S_{ij} = S_{ji}, \quad \Omega_{ij} = - \Omega_{ji}, \quad D_{ij} = S_{ij} + \Omega_{ij}$

$$\delta_{ij}D_{ij} = D_{ii} = \operatorname{div} C, \quad S_{ij}\Omega_{ij} = 0$$

We obtain $\quad (1/\rho)p_{ij}D_{ij} = (1/\rho)[- p\operatorname{div} C + 2\mu S_{ij}^2 - (2/3)\mu(\operatorname{div} C)^2]$

Let $\quad \Phi = \mu[2S_{ij}^2 - (2/3)(\operatorname{div} C)^2], \qquad$ then

$$(1/\rho)p_{ij}D_{ij} = - (p/\rho)\operatorname{div} C + \Phi/\rho \qquad (3)$$

In the equation, ϕ is the divergence function.

For power produced in this portion, we first notice that p, ρ, S_{ij} and div C are not related to the position of the observer. Hence, it can be considered that the deformation power is not related to the observer. Secondly, we know from the divergence definition formula div C = δ (dV)/dVdt of velocity C, -(p/ρ)div C = -p[δ (dV)]/ρ dVds. In the equation, δ (dV) indicates the variation on micro-element volume dV in dt. Hence, this term can be viewed as the micro-element compression power on a unit mass of gas by pressure.

47

LITERATURE

1. Liu Gaolian and Wang Jiasheng, Gas Dynamic Fundamentals of Turbomachinery, Mechanical Engineering Publishing Service, Beijing (1980), 15-18.

FLOW-FIELD LINE RELAXATION SOLUTION FOR S$_2$ RELATIVE STREAM SURFACE WITH THE SPLITTER BOUNDARY CONDITION*

Zhu Rongguo

Institute of Thermophysics Engineering, Chinese Academy of Sciences

Based on Wu's general three-demensional turbomachine flow theory, a computer program of flow field matrix line relaxation was established for flow along the relative stream surface S₁ of ducted fans in bypass engine.

It was the development of reference (3), and the splitter boundary condition of the fan compressor was considered and the structure of the computer program was improved.

I. FOREWORD

In a fanjet engine, the shape and position of splitters of internal and external inclusion can have a significant influence on performance of a fanjet engine. Hence, the understanding of the distribution of velocity and pressure of the splitter surface and the influence on the flow field have very important significance to raise the performance of a fanjet engine.

The computer program introduced in the paper adopts the fundamental equation set [1, 2] of turbomachinery three-dimensional flow gas dynamics with arbitrarily non-perpendicularly intersecting curve coordinates and the corresponding non-perpendicularly intersecting velocity component, as well as the flow field line relaxation numerical calculation method [3]. This is a development of the original S$_2$ stream surface counter problem

---

*The paper was read at the Third All China Engineering Thermophysics Conference at Guilin in April 1980.　　49

computer program [3]. The program considers the boundary condition of a splitter with internal and external inclusions; it is primarily used in gas dynamics design computation of the fan portion of the fanjet engine.

Compared with the original S_2 stream surface counter problem computer program, this program makes some effort in saving the internal memory storage capacity, thus computation nodal points are used, using only the internal memory from the originally allowed some 700 nodal points to some 1000 points without reducing the computation speed.

II. COMPUTATION EQUATIONS

(A) The principal equation to be solved: The principal equation to be solved is similar to that described in manuscript [3]; however, for saving internal memory capacity during computation, the equation is written into the following form:

$$\frac{\partial}{\partial x^2}\left[(V^1 + V^2 \sin(\theta_1 - \theta_2))\sqrt{a_{11}}\right] - \frac{\partial}{\partial x^1}\left[(V^1 \sin(\theta_1 - \theta_2) + V^2)\sqrt{a_{22}}\right]$$

$$= \frac{\sqrt{a_{11}}}{V^1}\left[-\frac{V_\theta r}{r^2}\frac{\partial(V_\theta r)}{\partial x^2} + \frac{\partial H}{\partial x^2} - T\frac{\partial s}{\partial x^2} - f_2\right]$$

We introduce the flow function variable ψ, definition $\partial\Psi/\partial x^2 = f\sqrt{a_{22}}\rho V^1$

and $\qquad \partial\Psi/\partial x^1 = -f\sqrt{a_{11}}\rho V^2$. In the equations,

$$f = 2\pi r(P - t)\cos(\theta_1 - \theta_2)/(\zeta \cdot P \cdot \xi_G).$$

Then the principal equation for solving the flow function is:

$$\frac{\sqrt{a_{11}}}{\rho f\sqrt{a_{22}}}\frac{\partial^2\Psi}{\partial(x^2)^2} - 2\frac{\sin(\theta_1 - \theta_2)}{\rho f}\frac{\partial^2\Psi}{\partial x^1 \partial x^2} + \frac{\sqrt{a_{22}}}{\rho f\sqrt{a_{11}}}\frac{\partial^2\Psi}{\partial(x^1)^2}$$

$$+ \left[\partial\left(\frac{\sqrt{a_{11}}}{\rho f\sqrt{a_{22}}}\right)\Big/\partial x^2 - \partial\left(\frac{\sin(\theta_1 - \theta_2)}{\rho f}\right)\Big/\partial x^1\right]\frac{\partial\Psi}{\partial x^2}$$

$$+ \left[\partial\left(\frac{\sqrt{a_{22}}}{\rho f\sqrt{a_{11}}}\right)\Big/\partial x^1 - \partial\left(\frac{\sin(\theta_1 - \theta_2)}{\rho f}\right)\Big/\partial x^2\right]\frac{\partial\Psi}{\partial x^1} = A + F.$$

50

In the equation, $A = \dfrac{\sqrt{a_{11}}}{V^1}\left[-\dfrac{V_\theta r}{r^2}\dfrac{\partial(V_\theta r)}{\partial x^2} + \dfrac{\partial H}{\partial x^2} - T\dfrac{\partial s}{\partial x^2}\right]$

and $\qquad\qquad F = \left[\dfrac{\partial(V_\theta r)}{\partial x^1} + \dfrac{\sqrt{a_{11}}V^2}{\sqrt{a_{22}}V^1}\dfrac{\partial(V_\theta r)}{\partial x^2}\right]\dfrac{\partial \varphi}{\partial x^2}.$

(B) Calculation of other parameters: The fundamental calculation formula is the same as the original S_2 program [3]. Several differences are explained in the following:

(a) Since the program is mainly used for gas dynamics calculation of the fan portion of a fanjet engine, the temperature increase is relatively small. Therefore, in the program it is specified that *the gas specific heat k is a constant*: the corresponding calculation equation of dimensionless temperature and density is $T = (H - V^2/2)/H_1$ and $\rho = T^{\frac{1}{k-1}}\cdot e^{-(s-s_1)}.$

In the equation, H_1 and s_1 are constants related to inlet conditions.

(b) By using the catching method solving for the value ψ of station j, since the value ψ of the root portion of the external inclusion part does not equal zero, the repeated derivation formula during calculation is changed slightly.

In the process of cancelling elements, in order to cancel elements in the equation
$$E1_k\Psi_{k-1} + E2_k\Psi_k + E3_k\Psi_{k+1} = B_k$$
and to rewrite into the standard form of $\psi_k + b_k\psi_{k+1} = g_k$. For k=2, we have
$$\psi_2 + b_2\psi_3 = g_2$$

then $\qquad\qquad \Psi_2 + E2_3\Psi_3/E2_2 = B_2/E2_2 - E2_1\Psi_1/E2_2.$

Correspondingly, we have $b_2 = E2_3/E2_2$ and $g_2 = B_2/E2_2 - E2_1\psi_1/E2_2.$

III. CALCULATION REGION AND SEQUENCE OF INTERATIVE SUBSTITUTION

The entire calculation is divided into two major regions: fan portion, internal inclusion portion, and external inclusion portion, as shown in Fig. 1.

The fan region is ABCFC'B'A'A; the internal inclusion region is EFG'D'C'B'E; and the external inclusion region is BCDGFEB. The last two j stations B'B and C'C in the fan portion, respectively, coincide with the first two j stations (B'E and C'F and EB and FC) of the internal and external inclusions. In other words, the BCFC'B'EB are, respectively, of two different calculation regions; this can be viewed as the corresponding points of two different mesh lattices. On these points, for different regions the geometric parameters, such as $\sqrt{\sigma_{r_1}}$, $\sqrt{\sigma_{r_2}}$, $\sin(\theta_1 - \theta_2)$ are different; however,

the physical quantities, such as $V_{\theta r}$, H, s and ρ, are the same. This way can be viewed as a simple method of local dual mesh lattices.
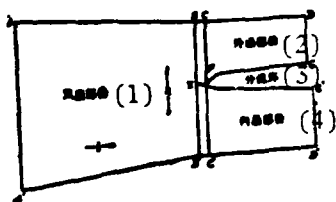
Fig. 1. Regional classification diagram of computation.
Key: (1) Fan portion; (2) External inclusion portion; (3) Splitter; (4) Internal inclusion portion.
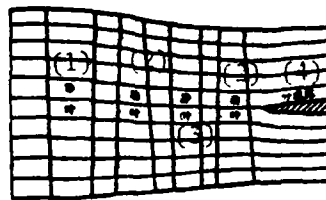
Fig. 2. Meridian streamline distribution of two stages of fans with splitter.
Key: (1) Guidance blades; (2) Moving blades; (3) Static blades; (4) Splitter.

During calculation, calculation is conducted on j stations in sequence from upper to lower streams for each region. In the fan region, the calculation is conducted on the B'EB station to transmit the physical quantities of the corresponding nodal points of mesh lattices of line B'B to the internal and external inclusion region. Then, calculation is conducted in sequence of j stations from C'F and FC lines of the internal and external inclusions until D'G' and GD are reached. The physical quantities calculated from C'F

52

and FC stations are transmitted to the corresponding nodal points of mesh
lattices on line C'C in the fan region. Thus, a complete repetitive substi-
tution is done until convergence if attained.

IV. COMPUTER PROGRAM AND TRIAL COMPUTATION

The computer program is compiled with ALGOL language in a TQ-16 computer
of 32K internal memory. The operating process of the computer program is
as follows:

(a) Input the original data, dimensionless parameters, and geometric
parameters at the nodal points of the calculation mesh lattice.

(b) The initial field for repetitive substitution calculation is given
before the repetitive calculation is conducted, including the transmitting
values between the fan region and internal and external inclusion regions.

(c) Accuracy inspection is done. If accuracy is not accepted, we
repeat (b) [calculation of other parameters, in II]. If the accuracy is
satisfied, the calculation result is given as an output printout.

The source program using ALGOL language is not presented here.

The program is used for trial calculation of some examples. One of
the examples is for the two stages fan of JT-3D. The result of trial
computation satisfies the program.

Figure 2 shows the meridian streamline distribution under the operating
condition of design points for the fan portion of JT-3D. Trial calculations
for changing the channel inclusion ratio were conducted. When the geometrical
shape remains the same while the internal inclusion flow is reduced, it is
obvious that the streamlines move toward the blade tip.

During repetitive substitution, the super relaxation factor $\alpha = 1-1.65$ is
adopted. For satisfying the engineering accuracy, it is enough to conduct

15-20 repetitive substitutions. The computer time required for computation is approximately 3-4 minutes.

LITERATURE

1. Wu Zhonghua, NACA TN 2604, 1952.

2. Wu Zhonghua, the Turbomachinery Three Dimensional Flow Gas Dynamics Fundamental Equation Set and Solving Method Using Non-perpendicularly Intersecting Curve Coordinate and Velocity Component, Proceedings of 3rd ISABE, 1976, 233-252; Jixie Gongcheng Xuebao [Journal of Mechanical Engineering], 15, 1 (June 1979).

3. Zhu Rongguo, The S_2 Stream Surface Counter Problem Flow Field Line Relaxation Solution Using the Non-perpendicularly Intersecting Curve Coordinate and Velocity Component, Gongcheng Rewuli Xuebao [Engineering Thermophysics Journal], 1, 1 (February 1980).

EFFECT OF CASING TREATMENT ON PERFORMANCE OF AN AXIAL COMPRESSOR*

Li Keming, Zhao Quanchun, and Sun Yuanying
Shenyang Aeroengine Research Institute

An experimental investigation was conducted, and is herein reported, to obtain the effectiveness of four treated casing configurations on performance of an axial compressor. Test shows that the surge margin and distortion tolerance for the axial compressor are improved by means of casing treatment, so that the circumferential pressure profile is further improved and the peak effeciency of the compressor is almost unaffected. There is a common trend for the four treated casings, that is the increment in surge margin at lowerspeed is greater than that at higher speed; the increment in surge margin with distorted inlet flow is more than that with uniform inlet flcw.

I. FOREWORD

With increased range of aircraft flight and the appearance of anomaly flow fields at the engine inlet, it is required to have sufficient distortion tolerance and surge margin capability for the compressor. The casing treatment is one of the effective measures of increasing distortion tolerance and surge margin.

The report introduces the principal results of a three stage super- and transonic *low pressure compressor* with experimental study [1] on casing treatment for the first stage rotor outer wall. Four types of casing treatment were designed and tested (small blade turbulent flow type, circumferential slot type, slant slot type, and turbulent flow type with stationary chamber). Tests were conducted on a homogeneous flow field, quasi-homogeneous flow field (with supporting frame), and stability state circumferential inlet distortion flow field. The experimental work was conducted at a compressor testing platform of the Shenyang Aeroengine Research Institute.

II. STRUCTURE CONFIGURATION OF CASING TREATMENT

Table 1 lists four types of structural configuration and parameters of casing treatment. The physical meaning of the parameters is shown in Fig. 1.

Table 1. Structure configurations and parameters of various types of casing treatment.

(a) 机匣型式	(b) 轴向位置	(c) 处理宽度 mm	(d) 与轴线夹角	(e) 打开面积比 %	(f) 径向角度	(g) 驻室高度 mm	(h) 其他
(i) 小 叶 片	(p) 伸出动叶 28mm	58	26°57'	70	30°	2.5	255 片圆周均布 (s)
(j) 周 向 槽	(q) 限于动叶核心	33.5	90°	70	0°	0	7 槽均布 (t)
(k) 斜 槽	限于动叶核心	32	117°3'	62	0°	17	360 片圆周均布 (u)
(l) 带驻室扰流式 (m) 大驻室	伸出动叶 34mm	58	10°	68.2	45°	12	250 片圆周均布 (v)
(n) 小驻室	伸出动叶 34mm	58	10°	68:2	45°	9.5	250 片圆周均布 (v)
(o) 轴向后移	伸出动叶 (19)mm	58	10°	68.2	45°	9.5	250 片圆周均布 (v)

Key: (a) Casing types; (b) Axial position; (c) Treatment width; (d) Included angle with the axial line; (e) Ratio of opening area; (f) Radial angle; (g) Height of stationary chamber; (h) Others; (i) Small blade; (j) Circumferential slot; (k) Slant slot; (l) Turbulent flow type with stationary chamber; (m) Large stationary chamber; (n) Slow stationary chamber; (o) Rear axial movement; (p) Extruded moving blades; (q) Limited to core of moving blades; (r) Extruded moving blades; (s) Uniformly distributed 255 blades at circumference; (t) Uniformly distributed 7 slots; (u) Uniformly distributed 360 blades at the circumference; (v) Uniformly distributed 250 blades at the circumference.
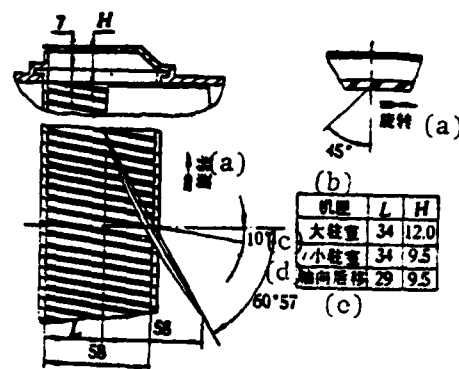
Fig. 1. Treatment casing structural
diagram of turbulent flow type with
stationary chamber.
Key: (a) Rotation; (b) Casing; (c)
Large stationary chamber; (d) Small
stationary chamber; (e) Axial rear
movement.

III. TESTING RESUTLS AND ANALYSIS

(A) Comparison of increment of distortion tolerance:

The increment Δ of distortion tolerance is calculated according to the
following formula:

$$\Delta = \left(\frac{R \times W'}{R' \times W} - 1 \right) \times 100\%$$

In the equation, R' and W' are the converted flows and pressure ratio of
the compressor distortion point of a standard casing.

Figure 2 shows the compressor characteristic curves of a standard casing
and turbulent flow type treatment casing with stationary chamber. Generally,
the variation rules are the same for the other types of treatment casing
compressor characteristic curves. Table 2 shows the increase of distortion
tolerance of various types of treatment casing compressors.

It is apparent from Table 2 that the increment of compressor distortion
tolerance of quasi-uniform flow field rated revolution speed is not much.

With reduction of revolution speed, the distortion tolerance increases appreciably; the greatest increase occurs in the treatment casing with stationary chamber.

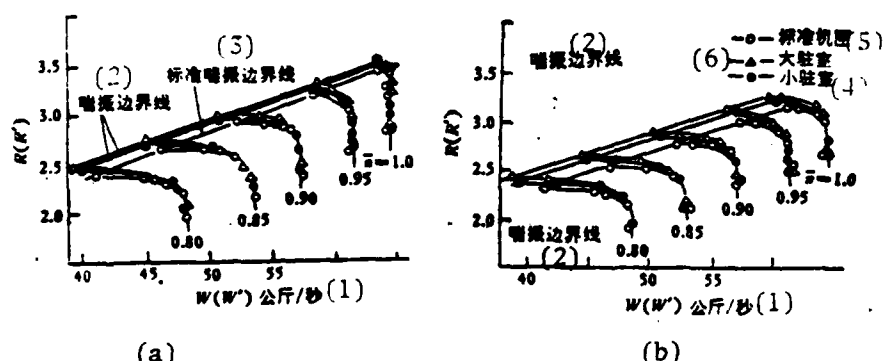(a)   (b)

Figure 2. Compressor performance of standard casing and turbulent flow type treatment casing with stationary chamber: (a) Quasi-uniform inlet flow field; (b) Circumferential surge inlet flow field for $\overline{D}=0.12$.
Key: (1) Kilograms per second; (2) Distortion boundary curves; (3) Standard distortion boundary curves; (4) Small stationary chamber; (5) Standard casing; (6) Large stationary chamber.

Table 2. Increments of compressor distortion tolerance of various types of casing treatment in contrast to standard casing.

(a) 进口流场 (d)机匣型式	(b) 准均匀进口流场 (e)扰流式			(i)小叶片	(j)斜槽	(k)周向槽	$\overline{D}=0.12$ 周向畸变进口流场 (c) (e)扰流式			小叶片(i)	斜槽(j)	周向槽(k)
	大驻室(f)	小驻室(g)	后移(h)				大驻室(f)	小驻室(g)	后移(h)			
△% z=0.80	6.7	5.7	6.0	2.3	5.4	3.0	8.7	5.9	7.1	4.8	4.9	2.7
z=0.85	3.5	3.6	3.4	1.6	2.4	3.3	6.7	4.6	7.4	4.2	4.3	2.1
z=0.90	2.9	2.4	2.9	1.9	1.8	2.2	6.1	3.6	6.1	4.7	4.0	2.2
z=0.95	0.8	0.5	—	1.4	1.8	1.2	5.1	3.8	—	2.7	2.8	2.0
z=1.00	0.8	0.5	0.8	0.9	1.3	1.1	5.0	3.9	1.5	1.5	1.2	0.5

Key: (a) Inlet flow field; (b) Quasi-uniform inlet flow field; (c) Circumferential surge inlet flow field for $\overline{D}=0.12$; (d) Casing type; (e) Turbulent flow type; (f) Large stationary chamber; (g) Small stationary chamber; (h) Rearward moving; (i) Small blades; (j) Slant slot; (k) Circumferential slot.

58

Several tests of inlet surge index were conducted on the treatment casing with small stationary chamber. At high revolution speed, the inlet surge index is increased, and the increment of compressor distortion tolerance also increases. This explains that casing treatment can raise compressor distortion tolerance at high revolution speed.

(B) Comparison of the maximum efficiencies

As revealed in the experimental results, for various types of inlet flow field, although the compressor efficiency curves vary for various types of treatment casing, the maximum efficiency values approach the compressor efficiency value of the standard casing.

(C) Comparison of compressor outlet pressure field:

In a circumferential surge flow field ($\overline{D}=0.12$), for a standard casing at the rated revolution speed, higher non-uniformity ($\overline{D}=8.7$ percent) of circumferential pressure exists. After adopting casing treatment, the non-uniformity of circumferential pressures at compressor outlet was significantly reduced, being more pronounced in a large stationary chamber ($\overline{D}=6.7$ percent). However, these only improved the outlet circumferential pressure field of the treatment sector without variation in the blade root region. For example, for the compressor outlet blade tip of a large stationary chamber, $\overline{D}=8.7$ percent of the standard casing was reduced to 4.9 percent.

IV. CONCLUSIONS

(1) Casing treatment can effectively increase compressor distortion tolerance and surge margin; the results are related to structural configurations. Size of the stationary chamber and axial position of the treatment sector can affect compressor performance. This explains that the structural configurations and parameters should be rationally selected.

(2) In various inlet flow fields, the maximum values of different casing treatment compressors approach the value of the standard casing.

(3) In a surge flow field, casing treatment can improve the outlet circumferential pressure field of the blade tip region at high revolution speed.

(4) The influences on increment of distortion tolerance of several casing treatments are the same. The influence is higher for low revolution speed than for high revolution speed; the influence of circumferential surge flow field is greater than the quasi-uniform flow field. This is the natural result with only the first stage casing treatment in a three stage axial compressor.

LITERATURE

1. Li Keming, Experimental Report of Casing Treatment on a Three Stage Low Pressure Compressor, Shenyang Aeroengine Research Institute, 1979, 7.

[2] Osborn. Walter, M.: George W., Jr.; and Heidelberg, Laurece J.: Effect of Several Porous Casing Treatments on Stall Limit and on Overall Performance of an Axialflow Compressor Rotor NASA TN D-6587 1971.

A CALCULATION METHOD FOR THE ROCKET ENGINE'S OPTIMUM THRUST NOZZLE CONTOUR DESIGN*

Tian Minhua

Combining the characteristic method with variation principle and applying it to supersonic flow field, a calculating method is presented for the optimum-thrust-nozzle contour design. This method can be used to design nozzle contours with various throat curvature radii and expansion area ratios. It is especially suitable for the design of nozzle contour with large expansion area ratio.

I. CALCULATION PRINCIPLE OF NOZZLE CONTOUR LINE OF OPTIMUM THRUST

Consider an ideal two-dimensional steady equal enthalpy flow without eddy. The flow field in the nozzles is axial symmetric. By using the cylindrical surface coordinate system, ABTE in Fig. 1 represents the intersecting curve between the nozzle contour surface and the meridian surface. The convergent sector $\widehat{AB}$ of the nozzle throat is the circular arc wall surface with R_1 as the radius of curvature. The initial expansion sector $\widehat{BT}$ at the lower stream of the throat sector is the circular arc wall surface with R_2 as the radius of curvature. The author and his colleagues selected a nozzle contour line $\widehat{TE}$ to have the maximum thrust produced at the nozzle with the given nozzle length L and environmental pressure p_a. This contour

---

61

line is called the "optimal thrust nozzle contour." A point C is selected at the axial line of the nozzle. Considering a control surface EC passing through point E at the outlet of the nozzle, this control surface $\widehat{EC}$ intersect at point D with the right characteristic line $\widehat{TH}$ passing through the nozzle exit point E (Fig. 1). The engine thrust R can be derived from the aerodynamic parameter of control surface EC.

$$R = \int_c^E \left[(p - p_e) + \rho v^2 \frac{\sin(\phi - \theta)\cos\theta}{\sin\phi} \right] 2\pi y dy \qquad (1)$$

(p, ρ, v, θ and ϕ indicate, respectively, the pressure, density, velocity, gas stream angle, and angle of inclination between the control surface and axis of the gas stream.)
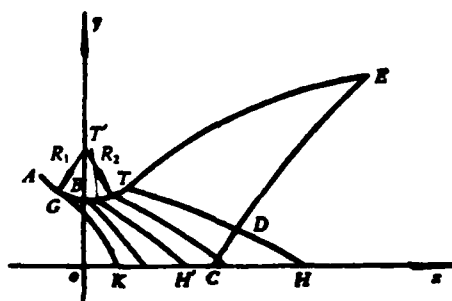
Fig. 1.

Since the point C is stationary, the nozzle length remains constant. Therefore, the nozzle length after C also remains constant, i.e.,

$$x_E - x_C = \int_c^E \text{ctg } \phi dy = \text{constant} \qquad (2)$$

In addition, because of continuity of flow, the flow passing through the control surface should be equal to flow G passing through the cross sectional area of the throat sector; i.e.,

$$G = \int_c^E \rho v \frac{\sin(\phi - \theta)}{\sin\phi} 2\pi y dy = \text{constant} \qquad (3)$$

62

The problem is then summarized into the situation that under the condition of equations (2) and (3), the thrust R of the nozzle attains the extreme value; i.e., the arbitrary function equation (1) attains the extreme value under the condition. By using the Lagrange product factor [1], the problem of extreme value under the condition is converted into the unconditional extreme value. By using the variable-difference method, the thrust R can attain the maximum value. The flow parameters on control surface EC should meet the various following conditions [1]: (Assume that the external pressure $p_a=0$)

(1) At the exit terminal point E, there is
$$\sin 2\theta_z = (2/\varepsilon M_z^2)\, \mathrm{ctg}\, \alpha_z \tag{4}$$

(2) At the control surface ED, there is the left characteristic line:
$$dy/dx = \mathrm{tg}\ (\theta+\alpha)$$

$$\frac{d\theta}{dx} - \frac{\mathrm{ctg}\,\alpha}{v}\frac{dv}{dx} + \frac{\sin\theta\sin\alpha}{y\cos(\theta+\alpha)} = 0 \tag{5}$$

(3) The flow parameters on ED also satisfy the two following relationship equations:

$$M^*\cos(\theta-\alpha)/\cos\alpha = M_z^*\cos(\theta_z-\alpha_z)/\cos\alpha_z \tag{6}$$

$$yM^2\left(1+\frac{\varepsilon-1}{2}M^2\right)^{-\frac{\varepsilon}{\varepsilon-1}}\sin^2\theta\,\mathrm{tg}\,\alpha = y_z M_z^2\left(1+\frac{\varepsilon-1}{2}M_z^2\right)^{-\frac{\varepsilon}{\varepsilon-1}}\sin^2\theta_z\,\mathrm{tg}\,\alpha_z \tag{7}$$

In the equations,
$$M^* = \left(\frac{1}{\varepsilon-1+2/M^2}\right)^{\frac{1}{2}}$$

(4) From continuity of flow, the following equation is apparently true:
$$\int_D^z \rho v\,\frac{\sin\alpha}{\sin(\theta+\alpha)}\,2\pi y\,dy = \int_D^T \rho v\,\frac{\sin\alpha}{\cos(\theta-\alpha)}\,2\pi y\,dx \tag{8}$$

(k, α, and M indicate, respectively, the adiabatic index, Mach angle and Mach number of the gas.)

II. GENERAL DESCRIPTION OF CALCULATION PROCESS

63

In nozzle design, generally the given initial conditions are R_1 and R_2 as the radii of the throat sector of the nozzle, gas adiabatic index k, and nozzle expansion area ratio A_E in order to obtain the optimal thrust nozzle contour. For nozzles of rocket engine, a smaller radius of curvature at the throat sector wall surface should be adopted in order to increase thrust and shorten the length. The author and his colleagues adopted the conformal curve coordinate method in manuscript [2] to calculate parameters of the transonic initial line GK (Fig. 1) at the nozzle throat sector. This method is simple in calculation and relatively high in accuracy; the method is adaptable to the situation of a relatively small radius of curvature at the throat sector wall surface. The entire supersonic flow field calculation relied on a characteristic line mesh [3]. For the left and right characteristic line equations, difference equations of two stage accuracy are adopted; i.e.,

$$dy/dx = \text{tg}(\theta^* \pm \alpha^*)$$

$$\Delta\theta \mp \text{ctg}\,\alpha^* \frac{\Delta v}{v^*} \pm \frac{\sin\theta^* \sin\alpha^*}{y^* \cos(\theta^* \pm \alpha^*)} \Delta x = 0$$

(Parameters with "*" indicate the average values for Δx.)

In the following, the derivation method (see Fig. 1) of the optimal thrust nozzle contour TE is described. From the characteristic line method, the flow parameters from the wall surface to the right characteristic line T'H' are derived item by item. We first assume a $M_E^{(1)}$; from equation (4), $\theta_E^{(1)}$ can be derived. Then a point D is sought on T'H' to satisfy equation (6). If point D is not on T'H', then the next right characteristic line is derived. If the point D is found, $y_E^{(1)}$ can be determined from eq. (7). In addition, parameters of various points on ED can be determined from eqs. (5-7). Moreover, by using eq. (8), we can determine whether T' is the point T of the separation point. If eq. (8) is not true, then the next right characteristic line T'H' and point D are derived until eq. (8) is satisfied. At that time, T'H' is the TH right characteristic line required. Again based on $y_E^{(1)}$, we derive $A_E^{(1)}$ to be compared with the given A_E. Usually, $A_E^{(1)}$ is not equal to A_E. By using the target shooting method, a suitable $M_E^{(n)}$ can be selected. We repeatedly use the above method until sufficiently approaching A_E.

64

Then, the right characteristic line TD and parameters on control surface ED are used as the initial condition, based on TE on the wall surface as the streamline. By using the characteristic line method, flow field parameters (Fig. 1) of the TDE triangular region can be calculated to obtain the optimal thrust nozzle contour TE.

III. CALCULATION RESULTS AND DISCUSSION

In the following, Table 1 lists (for different area expansion ratio A_E, and throat portion expansion sector radius R_2) parameters of separation point (point T) and the outlet terminal point (point E) parameters for the optimal thrust nozzle wall surface contour. In the table, L is the nozzle length; C_R is the nozzle thrust coefficient.

Table 1. $R_1=2$, k=1.23.

A_E	R_2	x_T	y_T	θ_T	L	θ_E	M_E	C_R
20	0.5	0.277	1.084	33°36'	8.399	13°10'	3.5147	1.7605
	1.0	0.551	1.165	33°25'	8.660	13°08'	3.5243	1.7606
	1.5	0.811	1.238	32°43'	8.907	13°06'	3.5326	1.7609
40	0.5	0.295	1.096	36°10'	13.301	11°36'	3.9985	1.8261
	1.0	0.585	1.189	35°49'	13.639	11°34'	4.0062	1.8264
	1.5	0.861	1.272	35°01'	13.955	11°33'	4.0128	1.8265
60	0.5	0.305	1.104	37°37'	17.276	10°49'	4.2903	1.8586
	1.0	0.604	1.203	37°11'	17.669	10°48'	4.2973	1.8588
	1.5	0.888	1.291	36°18'	18.032	10°47'	4.3031	1.8589

Considering the calculation results, for a certain area ratio, the smaller the radius R_2 of the expansion sector of the nozzle throat, the smaller is the nozzle length L. In order to shorten the nozzle length, we can appropriately reduce R_2; however, R_2 cannot be extremely small. Because the smaller the R_2, the larger is the expansion angle θ_T of the initial separation point. When R_2 is very small, the gas stream at the throat will expand exceedingly rapidly to increase loss of the gas stream. Therefore, experiments can solve the problem of what is the optimal value for a small R_2 value. Usually, the radius of curvature at the throat wall surface can be taken as $1 \leqslant R_1 \leqslant 2$ and $0.5 \leqslant R_2 \leqslant 1$.

LITERATURE

1. Rao, G. V. R., Exhaust Nozzle Contour for Optimum Thrust, Jet Propulsion, 28, 6, (1958), p. 377-382.

2. Jia Zhenxue and Lin Tongji, Transonic Hyperbola Contour Nozzle Flow, Lixue Xuebao [Mechanics Journal], 3 (1979), p. 199-208.

3. Sears, W. R., General Theory of High Speed Aerodynamics, Princeton Univ. Press, p. 583-669.

END

DATE
FILMED

7-83